Available online at www.sciencedirect.com

ScienceDirect

Geochimica et Cosmochimica Acta 221 (2018) 200–218

Geochimica et Cosmochimica Acta

www.elsevier.com/locate/gca

Rare earth element abundances in presolar SiC

T.R. Ireland [a,b,*], J.N. Ávila [a,b], M. Lugaro [c], S. Cristallo [d], P. Holden [a], P. Lanc [a], L. Nittler [e], C.M.O'D. Alexander [e], F. Gyngard [f], S. Amari [f]

[a] Research School of Earth Sciences, The Australian National University, Canberra ACT 2601, Australia
[b] Planetary Science Institute, The Australian National University, Canberra ACT 2601, Australia
[c] Konkoly Observatory, Hungarian Academy of Sciences, Budapest, Hungary
[d] INAF – Osservatorio Astronomico di Teramo, 64100, Italy
[e] Department of Terrestrial Magnetism, Carnegie Institution of Washington, Washington DC 20015, USA
[f] Laboratory for Space Sciences, Physics Dept., Washington University, St. Louis, MO 63130, USA

Received 10 December 2016; accepted in revised form 20 May 2017; available online 29 May 2017

Abstract

Individual isotope abundances of Ba, lanthanides of the rare earth element (REE) group, and Hf have been determined in bulk samples of fine-grained silicon carbide (SiC) from the Murchison CM2 chondrite. The analytical protocol involved secondary ion mass spectrometry with combined high mass resolution and energy filtering to exclude REE oxide isobars and Si-C-O clusters from the peaks of interest. Relative sensitivity factors were determined through analysis of NIST SRM reference glasses (610 and 612) as well as a trace-element enriched SiC ceramic. When normalised to chondrite abundances, the presolar SiC REE pattern shows significant deficits at Eu and Yb, which are the most volatile of the REE. The pattern is very similar to that observed for Group III refractory inclusions. The SiC abundances were also normalised to *s*-process model predictions for the envelope compositions of low-mass (1.5–3 $M_{\odot}$) AGB stars with close-to-solar metallicities ($Z = 0.014$ and 0.02). The overall trace element abundances (excluding Eu and Yb) appear consistent with the predicted *s*-process patterns. The depletions of Eu and Yb suggest that these elements remained in the gas phase during the condensation of SiC. The lack of depletion in some other moderately refractory elements (like Ba), and the presence of volatile elements (e.g. Xe) indicates that these elements were incorporated into SiC by other mechanisms, most likely ion implantation.

1. INTRODUCTION

Lanthanides of the rare earth element (REE) group play an important role in understanding the nature of geochemical processes. The elements La to Lu show a progressive increase in mass and ionic radius, but maintain similar trivalent chemistry because the electron configuration changes through the filling of the inner 4f shell. This characteristic generally results in smooth changes in abundance patterns in terrestrial rocks and minerals. Two exceptions are in the abundances of Eu and Ce. Eu can exist in the divalent state and can substitute preferentially for Ca^{2+} in Ca-bearing minerals such as feldspar, while Ce can become quadrivalent and can substitute preferentially in zircon for Zr^{4+}.

In cosmochemistry, the different volatilities of the REEs play an additional and significant role in elemental-abundance behaviour particularly in refractory inclusions, which have a high temperature origin in the earliest stages

* Corresponding author at: Research School of Earth Sciences, The Australian National University, Canberra ACT 2601, Australia.
E-mail address: trevor.ireland@anu.edu.au (T.R. Ireland).

http://dx.doi.org/10.1016/j.gca.2017.05.027
0016-7037/

of the Solar System (Ireland and Fegley, 2000; Amelin et al., 2010). Complex REE patterns that record nebula and/or parent body processes have been reported for calcium-aluminium-rich inclusions (CAIs). Mason and Taylor (1982) classified Allende inclusions into six groups based on these variations. For Group III inclusions, characteristic depletions in Eu and Yb are ascribed to these elements being the most volatile of the REE, and are the result of fractional condensation and isolation of the refractory inclusion from the gas, or through heating of ultrarefractory inclusions to temperatures above the evaporation temperature of Eu and Yb. For Group II inclusions, the abundance pattern shows a characteristic positive Tm anomaly with its abundance elevated above the neighbouring ultra-refractory heavy REE. This pattern can only be interpreted as being the result of fractional condensation because it requires the removal of the ultrarefractory heavy REEs prior to condensation of the light REEs and Tm (Boynton, 1975).

A similar high-temperature origin is proposed for the formation of mainstream SiC grains, whose highly anomalous isotopic compositions indicate an origin as condensates in outflows of low-mass carbon-rich asymptotic giant branch (AGB) stars (Bernatowicz et al., 1987; Anders and Zinner, 1993; Hoppe et al., 1994; Zinner, 1998, 2004). During the late stages of stellar evolution, the ejecta from these stars are enriched in heavy elements made by the slow neutron capture process (the *s*-process). The production of *s*-process nuclides takes place in the helium intershell, the region between the helium-burning and hydrogen-burning shells, where neutrons are released by (α, n) reactions on ^{13}C and ^{22}Ne during interpulse and thermal pulse phases, respectively. For slow addition of neutrons compared to the competing β-decay rates, the abundances of the nuclides are determined by their neutron capture cross sections at the relevant energies. This has been demonstrated by isotopic measurements of presolar SiC for light elements (e.g. Ti, Ireland et al., 1991; Hoppe et al., 1994; Alexander and Nittler, 1999; Nguyen et al., 2018), intermediate mass nuclides Sr-Zr-Mo (e.g. Nicolussi et al., 1998; Lugaro et al., 2003; Podosek et al., 2004; Liu et al., 2015) through to REE and neighbouring element isotope abundances (e.g. Ba, Zinner et al., 1991; Savina et al., 2003; Ávila et al., 2013a; Liu et al., 2014; Nd and Sm, Zinner et al., 1991; Eu, Ávila et al., 2013b; Gd and Dy, Ávila et al., 2016; Hf-W, Ávila et al., 2012).

Somewhat less attention has been paid to the nature of trace-element abundances in SiC and their implications for formation mechanisms. Amari et al. (1995) measured a variety of trace elements, including Ce and Nd, in individual SiC grains from the SiC-rich KJH separate (3–6 μm) of the Murchison CM2 meteorite. These workers found that depletions were apparent in elements whose compounds are more volatile than SiC and that Ce and Nd were systematically enriched relative to Ti (and V).

Yin et al. (2006) used a technique based on ICP-MS analysis of a slurry of a diamond (and silicon carbide)-rich residue from Murchison. The signal coming from this residue was primarily enriched in *s*-process nuclides suggesting that even though SiC was only a small component of the residue, it contained practically all of the trace elements in the Ba-Hf mass region. These workers measured all multi-isotope REE, although only upper limits were obtained for low abundance elements such as Sm, Eu, and Yb. Upper limits were also obtained for the abundances of mono isotopic (Pr, Tb, Ho, Tm) and near mono-isotopic REEs (La, Ce, Lu). Of interest to the current work is the apparent depletion of Yb relative to the adjacent ultra-refractory element Er found by Yin et al. (op. cit.), suggesting that some degree of volatility fractionation may be present in silicon carbide.

In this work we have measured, using secondary ion mass spectrometry, a complete REE abundance pattern for fine-grained SiC separated from Murchison. While a bulk mineral separate likely represents a combined sample of many stars with diverse nucleosynthetic and condensation histories, it has the advantage of providing sufficient mass for the low abundances of the rare earth elements. Concentrations of trace elements are also higher in the finer grained samples (e.g., Zinner et al., 1991; Amari et al., 1995). It is also relevant for obtaining an average *s*-process profile in terms of galactic chemical evolution.

In performing this work, we fully evaluate potential isobaric interferences in the REE mass region by measuring a continuous high-mass-resolution spectrum from mass 30 to mass 210 in a synthetic silicon carbide. This spectrum shows the production of molecular interferences that have important implications for isotopic measurements of silicon carbide.

2. EXPERIMENTAL TECHNIQUES

2.1. Samples

Reference materials NIST SRM 610, NIST SRM 612, and a synthetic SiC ceramic enriched with trace elements (Ávila et al., 2013a), were analysed to determine relative sensitivity factors of the REE, Ba, and Hf. A sample of pure synthetic SiC was also included in the mount to evaluate production of isobaric interferences. The mount consisted of large fragments of these materials set in a 25 mm round epoxy disk, ground and finally polished with a 1 μm diamond suspension.

We have previously used a mount containing SiC grains from the KJB fraction (Amari et al., 1994) for measuring isotope compositions of various REEs (Ávila et al., 2012, 2013a,b). In doing those measurements, a number of neighbouring elements were analysed and so a number of inter-element ratios were available already. In particular, these provide excellent constraints for abundance relationships between the light REEs. This mount is labelled KJB2.

A sample of SiC previously used for determination of isotopic compositions of micrometer-sized dust (Nittler and Alexander, 2003) was used for additional bulk analyses of meteoritic presolar SiC. This residue was prepared by CsF dissolution of Murchison and size-separated by centrifugation. Whereas Nittler and Alexander (2003) studied grains larger than 1 μm, the mount studied here, labelled DTM-SiC, contains densely packed smaller grains of SiC. The residue was deposited in an isoproponal-water suspen-

sion onto a gold foil pressed onto a quarter inch (6.35 mm) round plug. This plug was held in a 25 mm round Al disk that was loaded into the standard SHRIMP mount holder.

2.2. SHRIMP analysis

Mass spectrometric analysis was carried out on SHRIMP RG at The Australian National University. SHRIMP RG is a reverse geometry ion microprobe capable of ultra-high mass resolution (>30,000 $M/\Delta M_{10\%}$ with $\Delta M_{10\%}$ being the full-width of the peak at 10% peak height) while maintaining high transmission (Ireland et al., 2008; Ireland and Bukovanska, 2003). A schematic layout of the instrument is provided in Fig. 1; components referred to below are highlighted. The analyses carried out in this work comprise acquisition of automated high-resolution mass spectra, as well as higher mass resolution analyses of specific elemental isotopes (Ba, REEs, Hf).

SHRIMP RG is configured to have a primary beam of O_2^-, accelerated to 10 keV and for this work focused to a spot of ca. 25 μm. Primary beam intensity was maintained at around 3 nA. Secondary ions at sample potential (10 kV) are extracted to real ground potential. The secondary ion beam is focused through a series of extraction lenses to the source slit. The width of the source slit is selectable through positioning of a bar containing a series of fixed slits.

The SHRIMP RG mass analyser consists of three essential units: the QQH chamber, the magnet, and the electrostatic analyser (ESA). In the QQH chamber, two electrostatic quadrupole lenses (Q1, Q2) are used to cause lateral divergence in the secondary ion beam while maintaining beam height to pass through the magnetic sector. A detection system (QQH monitor) can be used to optimise the passage of the secondary ion beam through the source slit. The magnetic field is controlled by a new-generation FC4 controller capable of ppm level field control even during dynamic peak cycling. In the ESA chamber, two electrostatic quadrupole lenses (Q3, Q4) are placed before and after the ESA plates respectively. Q3 is an essential focusing element of the ion optical design and Q4 is used as a projection lens to the collector slit. An energy-defining slit with motorised control of position and width is located between Q3 and the ESA.

The magnet produces mass separation prior to the ESA and so the mass spectrometer can only operate as a single collector instrument. The secondary ion beam is focused through to the collector assembly that includes a single, continuously variable collector slit. The beam is then focused either on to an electron multiplier, or switched electrostatically into a Faraday cup.

2.2.1. Mass spectra

High-resolution mass spectra covering the range of mass 30 to mass 210 were obtained to assess molecular interferences in the REE mass range. The measurement of the low mass range enables the identification of molecules produced in the sputtering process and the potential

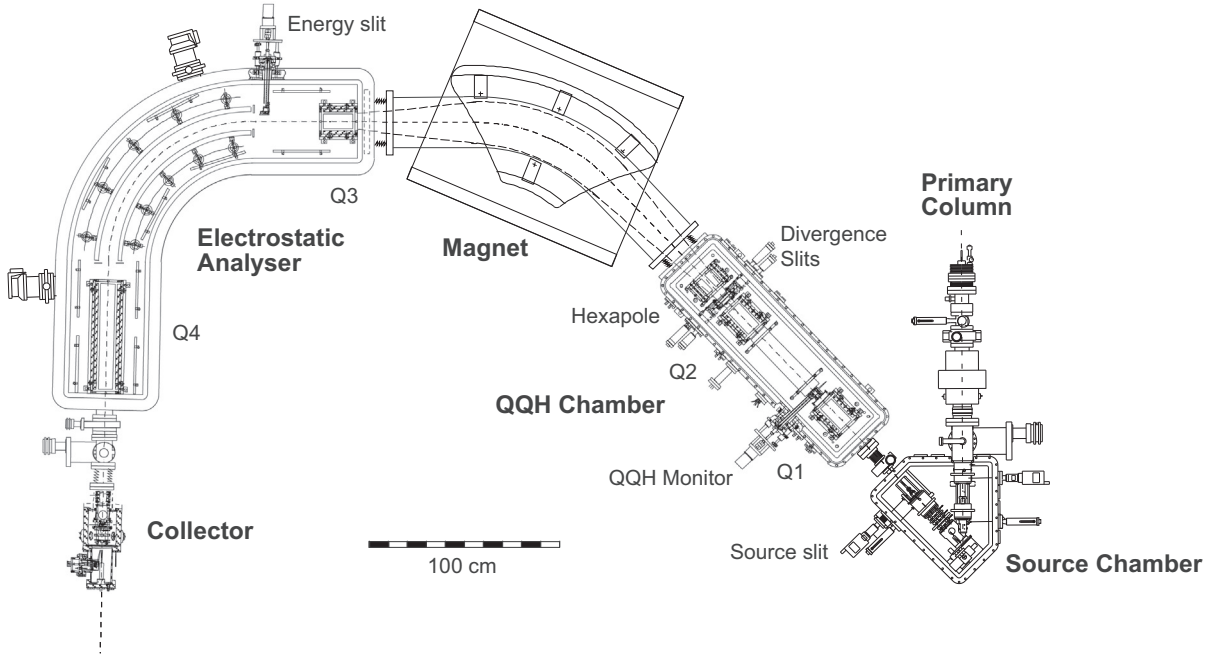

Fig. 1. Schematic layout of SHRIMP RG (after Ireland et al., 2008). SHRIMP RG is a reverse geometry mass spectrometer with the magnet preceding the electrostatic analyser. The feature of this design is the ability to operate at extremely high mass resolution by changing the *source slit*, and changing the *collector slit* width. This work utilises energy filtering which is achieved by placement of the *energy slit* preceding the electrostatic analyser. For secondary ion tuning without mass selection, as used for extended mass range mass scans (see Fig. 5), the *QQH monitor* can be inserted.

contribution of molecules to higher mass REE isotope analyses. It has previously been noted by Ávila et al. (2013a) that unresolvable mass interferences are present in the Ba mass region, and these interferences can be discriminated against by energy filtering (see e.g. Zinner and Crozaz, 1986). Therefore, high mass resolution spectra were also obtained for discrete energy offsets to assess discrimination of interferences with secondary ion energy.

The mass spectrometer was set to mass resolution $M/\Delta M_{10\%} \approx 5000$ with a 350 μm source slit and a 550 μm collector slit (Fig. 2). The high resolution spectra are carried out ca. 2500 steps per 10 amu (~0.004 amu/step) with acquisition time per step of 0.5 s. A mass spectrum of mass 30–210 comprises at least 45,000 discrete acquisitions, with total data acquisition time of around 400 min. Sputtering and tuning conditions will not stay constant over this length of time, and so we carried out discrete 10 amu scans that were then combined into a total mass spectrum. The positions of nineteen spots were preloaded into the acquisition table. A 10% overlap was added to each spot analysis, hence, the first analysis starts at mass 29 (going to mass 40), mass 39 to 50 for the second spot, etc. Each spot position was rastered with the primary beam for 1 min, and the primary beam optimised by adjusting the steering from the duoplasmatron and maximising the apparent primary beam current running through the sample holder. The secondary beam was tuned by optimising the signal detected in the QQH monitor. Alignment of the beam going from the QQH monitor to the collector was carried out on $^{29}Si^+$ prior to the full automated analysis. The focus of the mass spectrometer is field dependent and so a correction for focus based on potential applied to the Q2 lens was applied. A spline fit to the Q2 focal positions was made for selected masses between mass 6 and mass 270; the mass-field relationship was also calibrated by the selected peaks as well.

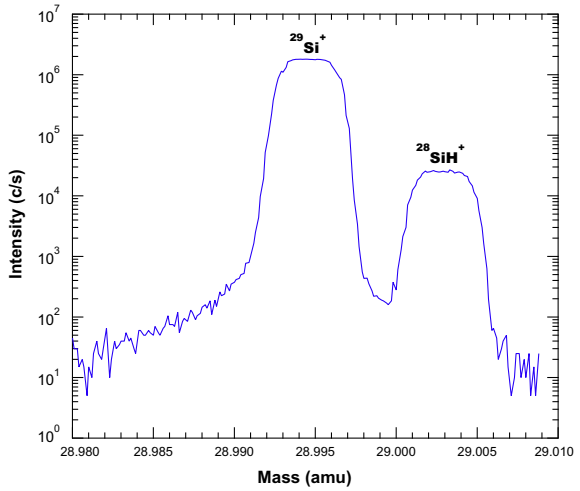

Fig. 2. Mass spectrum of $^{29}Si^+$ showing resolution from $^{29}SiH^+$ with $M/\Delta M_{10\%}$ (full peak width at 10% height) of ca. 5000 source slit = 350 μm; collector slit = 500 μm). This condition was used for extended mass scans (see Fig. 5). The extended tail evident on the low mass side of $^{29}Si^+$ is likely related to residual gas scatter in the mass spectrometer and equates to an abundance sensitivity of better than 10^{-4} at a mass offset of 0.01 am.

For mass spectra obtained with the energy offsets, the secondary ion beam was initially tuned to mass $^{29}Si^+$ in the collector prior to positioning the energy slit. The energy slit can be driven under computer control across the secondary ion beam energy focus over a range of 25 mm. The energy dispersion at the slit is approximately 8 eV/mm. The energy window can be opened up to 10 mm; for this work we selected an energy window of 5 mm (≈40 eV). SHRIMP RG is a double-focusing mass spectrometer and so the width of the energy window does not cause degradation of peak shape. However, scattered ions appear to be reduced with the narrower energy slit and so it was used to improve abundance sensitivity.

An energy scan of $^{29}Si^+$ is shown in Fig. 3. The unfiltered mass spectrum was obtained at the nominal ("nom") energy-slit position of 12.5 mm. Energy offsets were defined by two positions based on the $^{29}Si^+$ signal passing to the collector: a 50% peak height (at position 14.5 mm, i.e. 16 eV offset from nom), and a 10% peak height (at position 16 mm i.e. 28 eV offset from nom). For comparison, in the terminology of Zinner and Crozaz (1986) where the reference position is at the 10% low energy position on the peak (i.e. 9 mm in Fig. 3), the offsets would be approximately 40 eV and 52 eV respectively, although Zinner and Crozaz (op. cit.) used a 30 eV window, which affects the apparent offset.

2.2.2. Isotopic analysis

The presence of oxides in the mass spectrum requires a minimum mass resolution of approximately 8000 $M/\Delta M_N$ (where ΔM_N is calculated from the difference in the nuclidic masses) to resolve the light REE oxide species from the heavy REE atomic isobars. For isotope analysis in this work, a mass resolution $M/\Delta M_{10\%}$ of 12,000 and $M/\Delta M_{1\%\ \mathrm{of}}$ ca. 9000 (i.e. defined at 1% peak height) was used for isotopic analysis (Fig. 4). This was achieved by selecting a source slit width of 170 μm and closing the collector slit to 250 μm. This condition is sufficient to fully resolve light REE oxides from heavy REE atomic peaks as illustrated in Fig. 4 by the resolution of $^{141}Pr^{16}O^+$ from $^{157}Gd^+$ in NIST SRM 610. In addition, energy filtering was applied with a ca. 16 eV energy offset to discriminate against SiC cluster interferences.

The analytical run-table consisted of variations of 17 species including an isotope of each of the 14 stable REEs (typically $^{139}La^+$, $^{140}Ce^+$, $^{141}Pr^+$, $^{146}Nd^+$, $^{147}Sm^+$, $^{151}Eu^+$, $^{157}Gd^+$, $^{159}Tb^+$, $^{161}Dy^+$, $^{165}Ho^+$, $^{166}Er^+$, $^{169}Tm^+$, $^{172}Yb^+$, and $^{175}Lu^+$), as well as $^{138}Ba^+$, $^{138}Ba^{16}O^+$, and $^{180}Hf^+$. The isotope for each of the multi-isotopic stable REE was selected based on the abundance of the isotope and absence of atomic isobaric interference. The peaks of $^{138}Ba^+$ and $^{138}BaO^+$ species were both included. Ba is abundant in the SiC residues and so allows a signal normalisation to a relatively well known concentration, but also gives the possibility of an auto-center to monitor magnetic field drift. The $^{138}BaO^+$ species allows a mass calibration for the following heavy REEs. A measurement of $^{180}Hf^+$ was also included to close the *s*-process pathway.

The analysis of isotopic intensities at high mass resolution places extreme requirements on the control of the

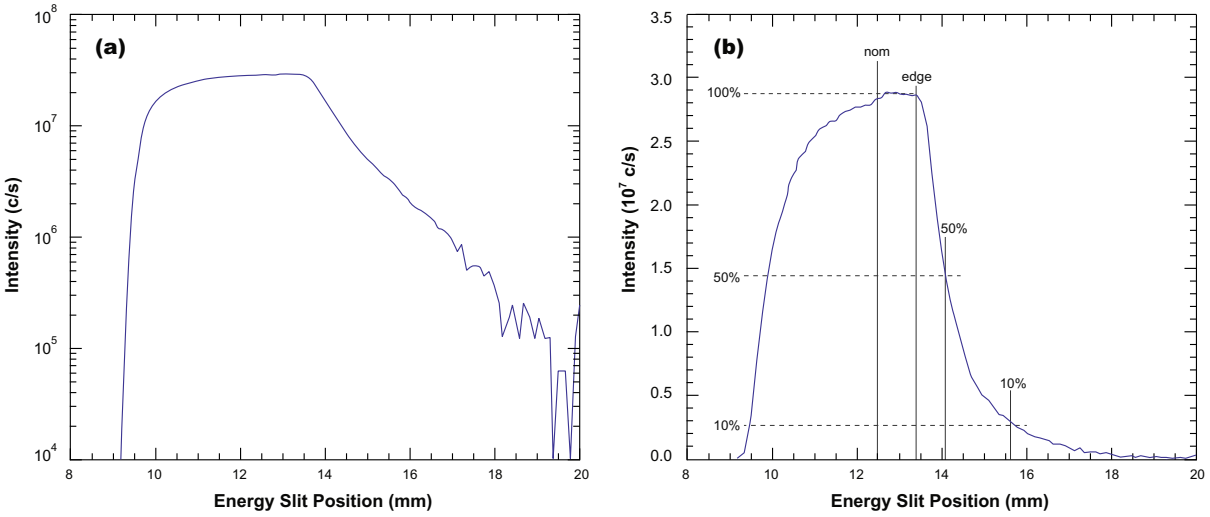

Fig. 3. Energy spectrum of $^{29}Si^{+}$ in (a) log scale, and (b) linear scale. SHRIMP RG is a reverse geometry mass spectrometer meaning that the energy (velocity) spectrum is actually a momentum (mv) spectrum for the specific peak detected at the collector immediately following the sector magnet. (a) The energy spectrum is quite similar in form to the energy spectrum derived from forward geometry instruments (q.v. Zinner and Crozaz, 1986). For energy filtering used in this work, we define the energy-slit positions "nom", being the nominal maximum position used for analysis without energy filtering, "edge" being the position from which the energy slit is set based on signal intensity: 50% being the position of 50% peak height, and 10% being the position of 10% peak height of the nominal maximum. For SiC extended mass scans, energy filtering has been set at nom, 50%, and 10% (Fig. 5). For energy filtering to remove polyatomic molecules in the mass region of the REE, the 50% peak height position was used. The calibration for the energy slit position to secondary beam energy is approximately 8 eV/mm (Ireland and Bukovanska, 2003). As such the offset indicated from "nom" to 50% is 16 eV and the offset from "nom" to 10% is 28 eV. The slit width used is 5 mm (40 eV).

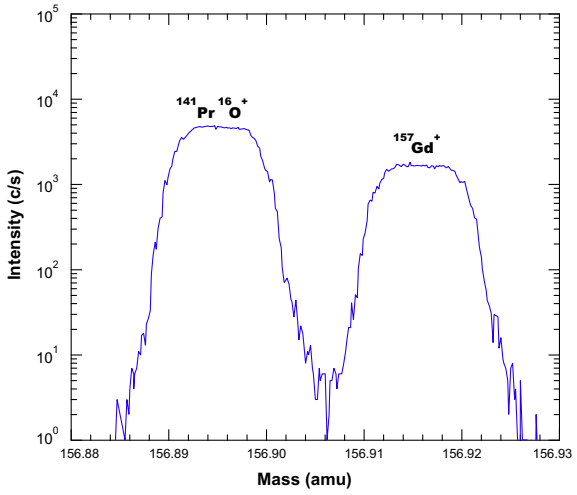

Fig. 4. High mass resolution spectrum of mass 157 from NIST SRM 610. $^{141}PrO^{+}$ is well resolved from $^{157}Gd^{+}$ with an energy offset of ca. 16 eV, mass resolution $M/\Delta M_{10\%}$ of ca. 12,000, source slit = 170 μm, collector slit = 200 μm). This condition was used to analyse isotopic compositions in the mass region of the REE.

mass-analyser magnet. The field controller must be capable of reproducibly landing on the peak flat top so as to provide accurate measurements. A typical run-table includes several peaks that can be used for centering and thereby define the hysteresis loop of the magnet. The reproducibility of the magnet was assessed through obtaining high signal intensities from the NIST SRM 610 glass, cycling through the mass stations, and centering on each of the peaks. Once settled, the relative peak shifts for each mass did not move by more than ±0.001 amu during the course of the analyses. For natural materials, the REE isotope signals were expected to be much lower than NIST SRM 610 and so centering was only carried out on $^{138}Ba^{+}$, $^{140}Ce^{+}$, $^{138}Ba^{16}O^{+}$; we then dropped the Ce peak-centering once a stable hysteresis loop was established. Measurement of $^{138}BaO^{+}$ avoids the need to center on a low-abundance heavy REE isotope peak, which has a neighbouring light REE isobar. If the oxide peak is larger than the atomic peak, there is a possibility of the signal from the side of the oxide peak exceeding the signal from the atomic peak and for the mass position to be shifted to the more intense oxide position. Field positions for each species following the centering peak were shifted according to the shift from the prior centered peak.

For the reference materials, an analysis consisted of five cycles through the run-table. Measurements of NIST SRM 610, NIST SRM 612, and the SiC ceramic were used to verify the stability of the analysis protocol. Following the stabilisation, measurements of the presolar SiC were interspersed with measurements of NIST SRM 610, NIST SRM 612, and the SiC ceramic. All isotopic analyses were carried out by ion counting on an electron multiplier.

For analysis of the NIST SRM 610, NIST SRM 612, and SiC ceramic, the start of the analysis was delayed by

60 s to allow the primary beam to burn through the ca. 15 nm gold coat, and to stabilise the secondary ion emission. The primary beam was checked for tuning manually. The secondary beam was then tuned automatically by using the QT1Y and QT1Z steering to maximise the $^{138}Ba^+$ beam. Then data acquisition commenced. The total acquisition time was ca. 10 min.

For analysis of the DTM-SiC mount, the primary beam was tuned on the gold substrate prior to placement on the SiC. After the primary beam was turned on, the analysis was carried out immediately so as to maximise the amount of material available for analysis. Initially for the thicker layers of SiC, the analysis provided suitable beam intensity, albeit decaying, for the whole analysis. For thinner layers it was found that SiC was sputtered through within ≈ 60 s and so the stage was stepped during analysis in order to maintain a suitable signal from SiC. This was monitored through the secondary beam monitor (SBM). This detector intercepts a small fraction of the total secondary ions and can be used to monitor emission of secondary ions from SiC, which is significantly higher than the emission from the gold substrate alone. The stage was moved prior to the measurement of $^{138}Ba^+$ and/or $^{138}BaO^+$. The change in secondary ion signal across the step was typically of the order of 10–20%. For this work, no correction was applied to the counts detected because of the small number of ions detected in the acquisition period.

3. RESULTS

3.1. Mass spectra of SiC

High-mass resolution spectra of pure synthetic SiC are presented in Fig. 5; base data are available as a supplementary file. The mass spectrum with 0 eV energy offset has a number of high intensity low mass peaks (Fig. 5a), extending from $^{30}Si^+$ to simple molecular peaks composed of Si-C-O. Species with intensities over 10^5 c/s include $^{28}Si^{12}C^+$ at mass 40, SiO^+ peaks at mass 44–46, $^{28}Si^{12}C_2^+$ species starting at mass 52, and Si_2^+, $SiCO^+$ at mass 56, and Si_2O^+ at mass 72. At higher masses there is a progressive decline in abundance of molecules towards the high mass end of the spectrum at mass 210.

The mass spectrum is dominated by cluster species of the general type $Si_xC_yO_z^+$. We have modelled the contributions of molecules with $x, y, z \leq 4$ for the isotopes ^{28}Si, ^{29}Si, ^{30}Si, ^{12}C, ^{13}C, and ^{16}O. Over 800 species are possible permutations of these species at masses below 210 amu. We have set aside additional potential molecules with ^{17}O and ^{18}O because these are relatively small contributions. Hydride species are also ignored; the hydride contribution is ≪1% of the Si metal species (based on the $^{28}SiH^+/^{29}Si^+$) and so is a small fraction of any peak in the mid to high mass range.

In the mass region of the REE (mass 140–180), a plethora of molecules are possible. For instance at mass 140, contributions from Si_5^+, Si_4CO^+, $Si_3C_2O_2^+$, $Si_2C_3O_3^+$, $SiC_4O_4^+$, and $C_5O_5^+$ are all possible isotopologues (based only on ^{28}Si, ^{12}C, and ^{16}O molecules). For mass 180, $Si_4C_3O_2^+$ and $Si_3C_4O_3^+$ are possible contributions. As noted by Ávila et al. (2013a), these molecules can be unresolvable (by mass) from Ba (and REE) species of interest and so must be excluded by energy filtering.

We have not attempted to identify specific contributions from these different isotopologues. However, we note that they are all complex molecules and as such are discriminated against by even moderate energy filtering. This is demonstrated in Fig. 5(b), which is a mass spectrum with a ca. 16 eV energy offset (based on energy window offset to 50% intensity of $^{29}Si^+$). In the mass 140 to mass 180 region only 6 counts were registered in a total of 5000 s total data acquisition, which is consistent with a background count rate of 0.001 c/s.

A residual contribution is apparent at and below mass 120 potentially corresponding to molecular clusters such as $Si_3C_3^+$, $Si_2O_4^+$, $Si_2C_4O^+$. On application of further energy filtering (ca. 28 eV based on 10% height of nominal $^{29}Si^+$), mass 120 clusters are still apparent but the counts are significantly reduced down to ≈ mass 75 where triatomic molecules start to become significant contributions (Fig. 5c).

It is therefore clear that clusters of Si, C, and O can be significant contributors to even high mass regions. Molecules formed from Si and C are indeed expected as these are major components of the matrix. It is interesting that O constitutes a significant constituent. Some oxide may be present, both as oxide minerals and surface contamination, but it is likely that a significant source of oxygen is from implantation from the primary O_2^- ion beam. If this is the case, there may be some time dependence of O-bearing molecular ion species in these spectra because of the likely build up of implanted oxygen until it attains a quasi equilibrium related to implantation and sputtering.

3.2. Isotope analysis of reference materials

Initial peak set up was performed on NIST SRM 610, which has nominal 400 ppm concentrations of Ba-REE-Hf. Count rates ranged from 18,000 c/s for $^{138}Ba^+$ to 750 c/s for $^{180}Hf^+$. Count times of 2–4 s were initially set for the selected peaks based on the abundance of the selected isotope (2s for $^{138}Ba^+$, $^{139}La^+$, $^{140}Ce^+$, $^{141}Pr^+$, $^{151}Eu^+$, $^{157}Gd^+$, $^{159}Tb^+$; 4s for $^{146}Nd^+$, $^{147}Sm^+$, $^{161}Dy^+$, $^{166}Er^+$, $^{172}Yb^+$, and $^{180}Hf^+$) in order to ameliorate the differences in total counts collected. The same counting times were used for NIST SRM 612 (nominal 40 ppm of Ba-REE-Hf).

The trace-element enriched SiC ceramic (JA-SiC) has a range of REE concentrations ranging from 0.055 μg/g for Tb to 522 μg/g for La, a Ba concentration of 3054 μg/g and Hf concentration of 1.21 μg/g (Ávila et al., 2013a). Count times used for the NIST SRM glasses were maintained for the analysis of JA-SiC.

Each analysis consisted of five cycles through the run table. Initially for NIST SRM 610 and 612 analyses, all peaks were centered during analysis. However, the centering was not possible for all peaks during analysis of JA-SiC because of the low abundance of some of the heavy REE. For analysis of JA-SiC, only $^{138}Ba^+$ and $^{138}BaO^+$ were centered in each cycle, with a field shift applied to the other peaks depending on the previous field shift of $^{138}Ba^+$ or $^{138}BaO^+$. Reproducibility of the peak positions

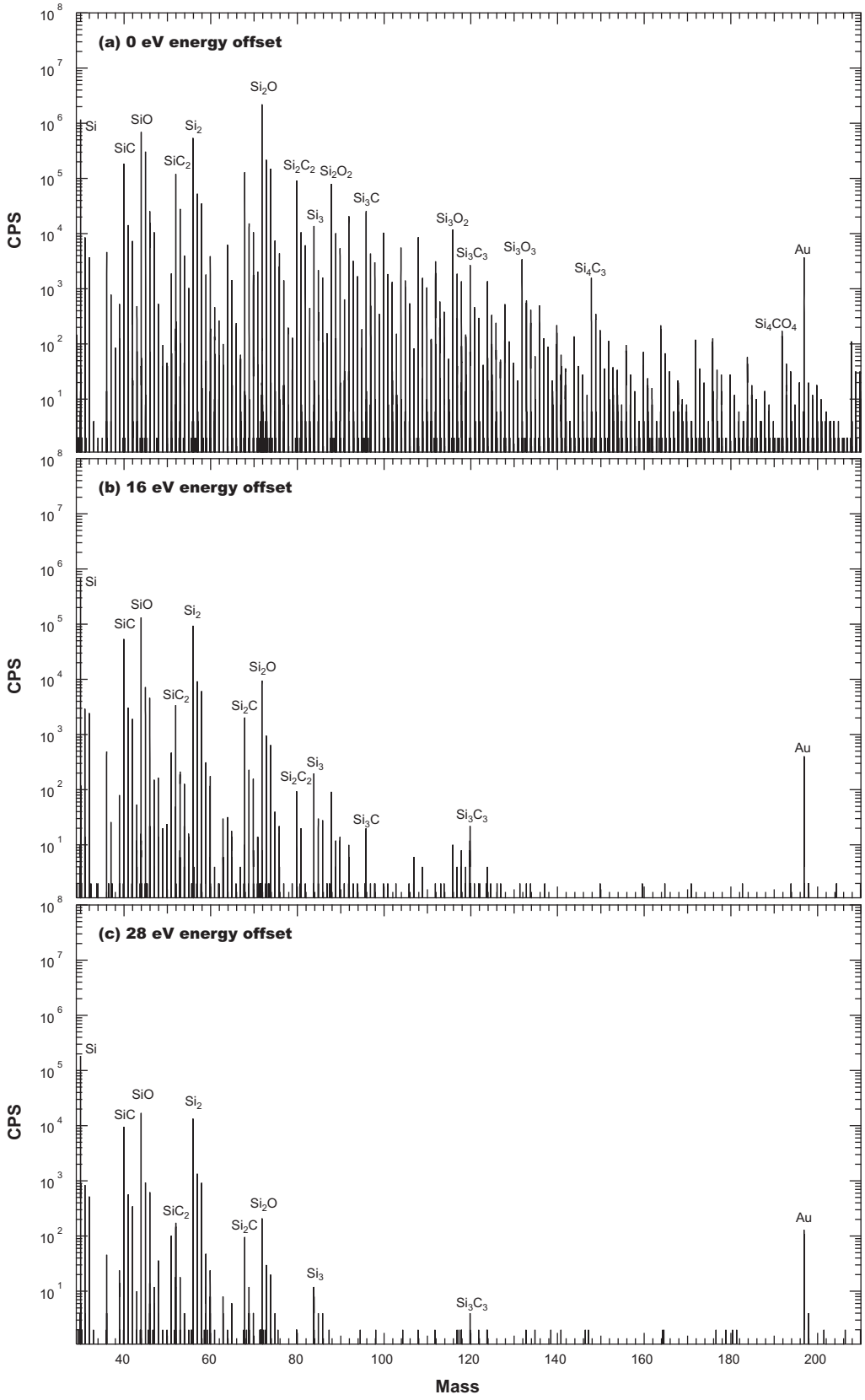

Fig. 5. Extended mass spectra from a synthetic SiC sample showing production of molecular ions out to high mass regions. Molecular ions consist of variable numbers of Si, C, and O atoms. (a) 100% energy slit transmission of $^{29}Si^{+}$, i.e. no energy offset; (b) 50% beam transmission (i.e. 16 eV energy offset); (c) 10% energy transmission (i.e. 28 eV offset) (q.v. Fig. 3). The molecular and cluster ions evident at all masses in (a) are progressively reduced with higher energy offset relative to $^{30}Si^{+}$ and simple molecular species. Suggested species correlating to the masses are shown.

within any cycle was noted to be typically of the order of 0.001 amu, well within the peak flat top. Reproducibility over a full analysis for all peaks was better than 0.003 amu, still well within the peak flat top. Analyses of NIST SRM 610 and NIST SRM 612 with a full centering routine and analyses with centering only on Ba and BaO species showed no discernible differences. NIST SRM analyses with no peak centering following measurements of JA-SiC were also consistent with the other NIST SRM analyses with auto-centering.

3.3. Determination of relative sensitivity factors

A Relative Sensitivity Factor (RSF) for each element is used to transform measured ion intensity ratios into elemental abundance ratios. For this work we have chosen the formulation whereby the ion ratio is divided by the RSF to yield the abundance ratio. Typically a major element (e.g. Ca or Si represented as ^{42}Ca or ^{30}Si) is used as a reference because its abundance can be determined by an independent technique such as electron microprobe analysis. Then the concentration of any element can be determined based on the ion ratio of the element of interest and an isotope of the reference element, assuming terrestrial isotope ratios. However, the mass position of a Si isotope is much lower than the mass range of the REEs and so artefacts related to the hysteresis loop of the magnet could cause peak drift. We could also use a mass-appropriate molecular species, but the energy filtering removes any molecules from the mass region of the REEs.

For this work we have determined RSFs for all REEs relative to $^{138}Ba^{+}$ (Table 1). This isotope was selected because Ba is abundant in all of the reference materials (NIST SRM 610, NIST SRM 612, and JA-SiC), as well as in the presolar SiC. We have chosen not to normalise to the abundance of Ba in the residue, but rather maintain it as a reference and normalise the ratios to solar abundances for the REE and Hf. The RSF for the reference materials are plotted in Fig. 6. NIST SRM 610 and NIST SRM 612 show equivalent RSF values. The uncertainties on the individual measurements of NIST SRM 610 are typically around 0.5% and those for NIST SRM 612 are around 2%, consistent with there being an order of magnitude higher concentrations in NIST SRM 610. The reproducibility of the ion ratios is typically 1–2% for NIST SRM 610 and 1–3% for NIST SRM 612. In both reference materials, the better reproducibility is associated with the light REE (La-Eu) as compared to the heavy REE (Gd-Lu). The uncertainties are close to counting statistics but for the light REEs they are likely limited by small variations in the primary beam intensity.

The pattern of relative sensitivity factors for NIST SRM glasses in Fig. 6 is similar to those we have obtained previously on SHRIMP RG (e.g. Liu et al., 2009; Tian et al., 2011), and to normalisations on Cameca instruments (e.g. Ireland, 1995, Fig. 18). All these patterns show a peak in the RSF value at Eu with a near systematic increase in RSF from La to Eu then a progressive decrease from Eu to Lu. This suggests that the RSF values for oxides, phosphates, and silicate glasses are related to the sputtering of these mineral matrices and that the REEs behave coherently as a group.

The RSF values determined for the JA-SiC reference material show substantially more variability than the NIST SRM silicate glasses. The light REEs La, Pr, Nd, Sm, and Eu show reproducibility at the 10–20% level; Ce is anomalous with over 30% variability. The variability in the heavy REEs ranges from under 20% for Yb, to 80–120% for Tb to Er. The light REEs have substantially higher concentrations (ranging from 60–500 μg/g) while the heavy REEs are all <16 μg/g, with Tb the lowest at 0.055 μg/g. However, the scatter is beyond being due simply to counting statistics. Ion count rates are highly variable from scan to scan. This is likely due to the methods used to produce the SiC ceramic. After mixing the component oxides and carbides, the charge was fused for only 30 min to avoid migration and nucleation of incompatible components. As such, very fine scale (nanometer) heterogeneities are likely present due to incomplete mixing and these are detectable during ion microprobe analysis.

Despite the heterogeneities apparent in the data from JA-SiC, it is apparent from the overall pattern of the

Table 1
Relative Sensitivity Factors (RSF).[a]

Isotope (REE/^{138}Ba)	Element	NIST-610	SD (%)	NIST-612	SD (%)	SiC ceramic	SD (%)
139	La	0.444	0.23	0.487	1.21	0.496	14
140	Ce	0.429	0.03	0.435	1.82	0.678	34
141	Pr	0.523	0.02	0.528	1.01	0.579	14
146	Nd	0.541	0.84	0.562	1.70	0.601	12
149	Sm	0.610	0.65	0.642	1.47	0.597	12
151	Eu	0.671	0.58	0.730	1.72	0.690	12
157	Gd	0.456	1.35	0.459	1.54	0.380	35
159	Tb	0.417	1.09	0.449	1.82	0.299	76
163	Dy	0.456	0.79	0.456	2.73	0.431	82
165	Ho	0.416	1.79	0.429	1.64	0.646	84
166	Er	0.396	1.89	0.391	2.57	0.413	118
169	Tm	0.416	1.42	0.404	2.00	0.350	52
172	Yb	0.402	1.46	0.409	1.49	0.387	18
175	Lu	0.245	1.74	0.245	1.23	0.306	39
180	Hf	0.079	1.38	0.085	2.08	0.305	47

[a] RSF as used in this work is defined as the ion ratio divided by the true ratio in the material.

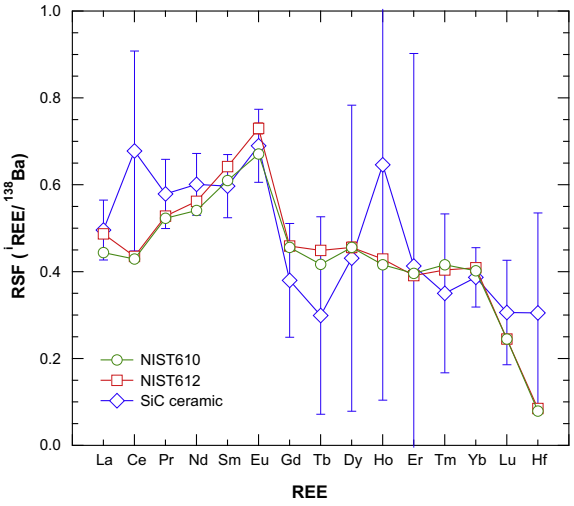

Fig. 6. Relative Sensitivity Factors (RSF) for REE relative to Ba in NIST SRM 610 and NIST SRM 612 silicate glasses and the synthetic silicon carbide ceramic (JA-SiC; Ávila et al., 2013a). RSF is defined as the ion ratio divided by the true ratio in the material. JA-SiC has heterogeneous REE concentrations leading to quite large uncertainties for any given element. Furthermore, some of the heavy REE have very low abundances, leading to large uncertainties for determinations of RSF. However, there is a good overall agreement between the RSF values for NIST SRM silicate glasses and the JA-SiC for La, Pr-Eu, and Gd, Yb, and Lu indicating that the well-determined RSF values for NIST 610 glass can be applied to silicon carbide. Error bars correspond to the standard deviation of the measurements (1SD). Error bars for analyses of NIST SRM 610 and NIST SRM 612 are smaller than symbols.

RSF values (Fig. 6) that the values for silicon carbide agree within uncertainty with those of the silicate glasses. This is consistent with the observation by Ireland and Bukovanska (2003) that the matrix effects apparent between different mineral species are largely related to normalisation to major elements. That is, the relative ionisation efficiencies of trace elements are consistent, and the normalisation to Ba removes the matrix effect that would be apparent if for example, the normalisation was based on an isotope of silicon. With the general agreement of the RSF determinations, we adopt the RSF values of NIST SRM 610 for the assessment of REE concentrations in the presolar silicon carbide.

For some analyses of the heavy REEs, we have adopted a limited run table in order to shorten the analysis time, and to optimise the peak centering routine. This run-table includes only $^{138}BaO^{+}$ as a reference species. As such, to combine the $^{138}Ba^{+}$ normalised data to the $^{138}BaO^{+}$ normalised data, we must determine the $^{138}Ba^{+}/^{138}BaO^{+}$ ratio for silicon carbide measurements.

Despite the heterogeneities apparent in the JA-SiC reference material, the Ba/BaO is very consistent. A mean of eight measurements gives a $^{138}BaO^{+}/^{138}Ba^{+}$ of 0.0669 (±0.0023; 1 standard deviation). This is notably different from the value obtained from the NIST SRM glasses. Six NIST 612 analyses give a mean of 0.136 (±0.004; 1 std. dev.). The elevated BaO/Ba in the silicate glass is likely related to the presence of oxygen in the silicate matrix, whereas the oxygen available in the SiC analysis is derived mainly from the oxygen primary ion beam.

3.4. Isotope measurements of presolar SiC

Part of the data set we have assembled is based on a number of ongoing measurements of KJB. These have been the result of isotopic analyses of the Ba-Pb mass region (e.g., Ávila et al., 2012, 2013a,b; Ávila et al., 2016). Isotope and inter-element ratios relative to $^{138}Ba^{+}$ and/or $^{139}La^{+}$ have been obtained from KJB2 for $^{140}Ce^{+}$, $^{141}Pr^{+}$, $^{149}Sm^{+}$, $^{151}Eu^{+}$, $^{153}Eu^{+}$, $^{157}Gd^{+}$, $^{163}Dy^{+}$, and $^{166}Er^{+}$. These data are based on between 2 and 24 individual analyses. Data were collected under similar operating conditions (>8000 $M/\Delta M_{10\%}$) and energy offset of 21–24 eV for analysis of Ba, La, Ce, Pr, Eu, Gd, Dy, and Er. Elemental ratios are determined to better than 10%, except for Pr and Er which are better than 20%. The measurements of the KJB2 SiC produces stable secondary ion intensities throughout the course of the measurement. The KJB2 mount has a relatively "thick" layer of SiC such that secondary intensities can be maintained for the order of ten minutes.

In order to better constrain the heavy REE abundances we have performed a number of measurements on a different mount with different characteristics. Fine-grained SiC on the DTM-SiC mount (Nittler and Alexander, 2003) was deposited in thinner layer than those on the KJB2 mount. In terms of the measurements presented here, the grains are thus sputtered away more quickly and as such analyses are subject to sample exhaustion. In the first measurement session, we measured Ba, BaO, Hf, and all the REE isotopes in regions where it was apparent there was a significant concentration of SiC. Following analyses of these few thick regions, we focused on obtaining heavy REE abundances, first by increasing the collection time on specific isotopes, and then by only measuring BaO and specific heavy REE.

Due to sample exhaustion, we attempted to extend the ion signal by moving the sample stage during the analysis, typically by around one half spot width per cycle. This does provide extended signal, but at the expense of an abrupt change in the count rates. The jump is typically 0–20% and so has a limited effect on the abundances determined from the single-digit (i.e. <10) counts acquired. This method was used to improve counting statistics for determinations of Tb, Ho, Tm, Yb, and Lu. Further, abundance ratios were determined relative to the BaO^{+} peak, which were then recalculated to the Ba^{+} for comparison with the light REE abundances. Abundance ratios were formed by taking the ratios of the total counts for the REE and Ba (or BaO), and errors calculated based on Poisson counting statistics.

3.5. Trace element abundances in SiC

A summary of the Murchison silicon carbide data is presented in Table 2. Data from the presolar SiC, normalised to ^{138}Ba and solar abundances, is illustrated in Fig. 7. Overall the pattern shows a relatively smooth decrease in REE

abundance to Ho and then an apparent rise in the abundances of Lu and Hf. Eu and Yb show significant depletions relative to the elemental abundances around them. Eu is depleted by approximately a factor of three, and Yb is almost an order of magnitude lower than Lu. The Tm abundance appears marginally high compared to the trend from Er to Lu.

Some of these attributes are apparent in trace element abundances in refractory inclusions from carbonaceous chondrites. A REE pattern depleted in Eu and Yb is very similar to that in Group III Allende inclusions (Mason and Taylor, 1982), and in platy hibonite crystal fragments (PLAC, Ireland et al., 1988; Ireland, 1990). On the other hand, a Tm anomaly is commonly attributed to Group II inclusions (Mason and Taylor, 1982) whereby it is postulated that an ultra-refractory component has been removed from the precursor. In this scenario, Tm appears anomalous because it behaves with a volatility similar to the light REE. These features will be discussed further in the following section.

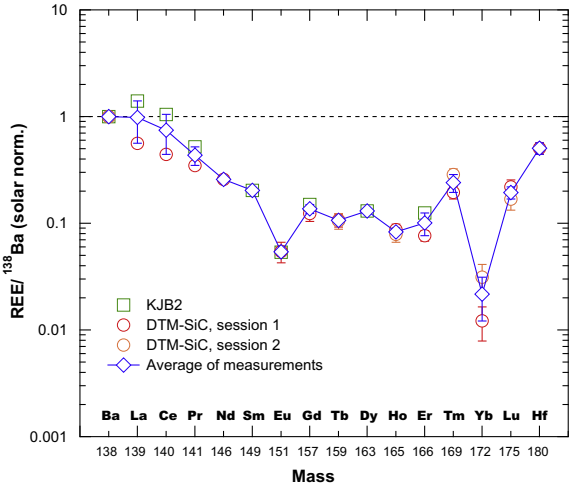

Fig. 7. Trace element abundances in meteoritic SiC normalised to solar abundances and Ba. The abundances show a smooth decline from La to Ho with a potential increase from Er to Hf, and, significant depletions in Eu and Yb. The decline in abundance from Ba is due to the large *s*-process contribution close to the $N = 82$ magic neutron peak (^{138}Ba). Significant depletions are apparent in the most volatile of the REE, Eu and Yb. This is likely due to incomplete condensation of Eu and Yb during condensation of the SiC grains. Solar abundances used for normalisation from Lodders (2003).

4. DISCUSSION

4.1. The *s*-process

Neutron addition to Fe group elements is the key foundation of the production of heavy elements. The addition of a neutron is followed by the competing probabilities of the addition of another neutron, or the potential for a β decay of a resulting nuclide if it is radioactive. If the β decay rate is not competitive, the nuclide simply adds another neutron (n, γ). Ultimately, a radioactive isotope is formed and a β decay changes the Z number as one of the neutrons decays into a proton. Thus, the *s*-process systematically follows the valley of stability of the chart of the nuclides through to the isotopes of Pb, and ultimately the heaviest stable nuclide ^{209}Bi.

Abundances on the *s*-process path are defined by the nuclear capture cross sections of the (n, γ) reactions, which determines the probability of any given isotope accepting a neutron. Reaction rates are temperature dependent and can cover a range of 5–100 keV for various He-burning scenarios, however a reference temperature of 30 keV is generally adopted to facilitate comparisons between models (Bao et al., 2000). Abundances are also related to the magic number peaks on the chart of the nuclides, corresponding to closed neutron shells, which have very low neutron capture cross sections. State of the art of the Maxwellian-averaged cross-sections (MACS) at kT = 30 keV versus atomic mass for the REE is shown in Fig. 8. For a few REE, the stellar temperatures are high enough for a significant population of low-lying excited nuclear states, which modify the neutron capture cross-sections measured from the laboratory. These effects are considered in the stellar MACS with the so-called stellar enhancement factor (SEF, Fig. 8c).

Table 2
REE isotopic abundance ratios in Murchison SiC-enriched bulk samples.

Isotope (REE/^{138}Ba)	Element	KJB2 (average)	Err (%)	DTM-SiC (session 1)	Err (%)	DTM-SiC (session 2)	Err (%)
139	La	0.19768	0.9	0.07928	2.7		
140	Ce	0.34739	0.8	0.14663	2.0		
141	Pr	0.02899	8.3	0.01938	4.9		
146	Nd			0.01187	4.6		
149	Sm	0.00229	5.0				
151	Eu	0.00078	3.3	0.00079	22		
157	Gd	0.00250	4.5	0.00206	16		
159	Tb			0.00203	14	0.00200	17
163	Dy	0.00402	3.7				
165	Ho			0.00251	13	0.00227	16
166	Er	0.00344	10	0.00211	11		
169	Tm			0.00231	13	0.00340	13
172	Yb			0.00021	35	0.00054	32
175	Lu			0.00245	16	0.00188	21
180	Hf			0.00967	12		

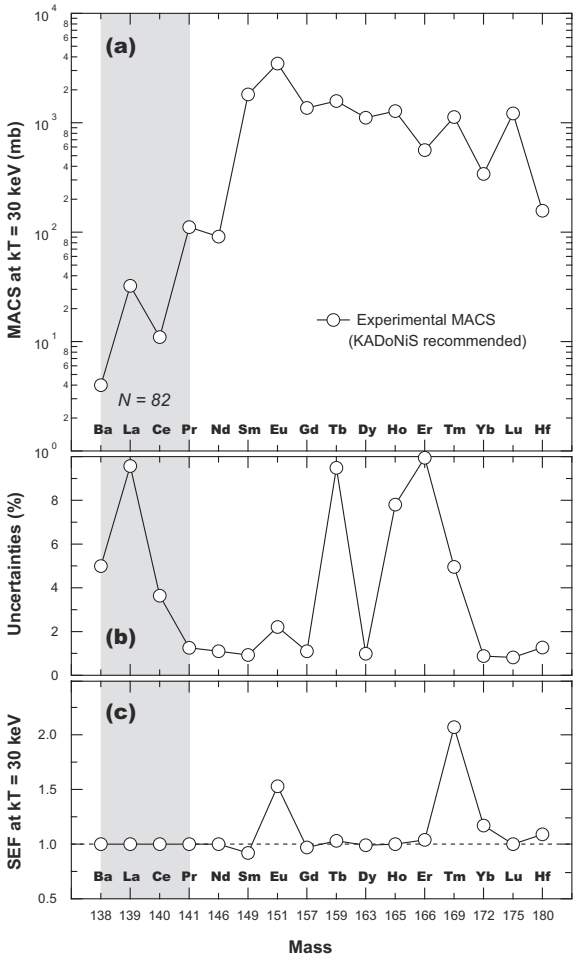

Fig. 8. (a) Maxwellian-averaged (n, γ) cross-sections (MACS) at 30 keV for rare earth elements discussed in the text. The (n, γ) cross-sections are taken from the KADoNiS database (v0.3). Grey area correspond to nuclides with neutron-magic number $N = 82$. (b) Neutron capture cross-section uncertainties at 30 keV. (c) For some nuclides it is necessary to multiply the cross sections by the stellar enhancement factor (SEF) at stellar temperatures of interest. The SEF take into account the thermal population of low-lying nuclear excited states at astrophysical temperatures and can impact the abundance of some nuclides. Stellar enhancement factors (SEF) are taken from the KADoNiS database.

Stars of spectral type MS, S, SC, and C have atmospheres that are rich in carbon and *s*-process elements. These are relatively low mass stars of 1–3 $M_{\odot}$ and are strong dust producers in the Galaxy. They commonly display the 11.3 μm SiC emission band, which is not surprising since SiC is a major condensate formed at C/O > 1. The *s*-process nuclides are also apparent in the photospheric emission from these stars which show strong enrichments in Zr, Mo (at magic $n = 50$ peak), and Ba, La (at magic $n = 82$), and also in the radionuclide ^{99}Tc ($t_{1/2} = 0.2$ Ma), attesting to the active *s*-element production in these stars.

The *s*-process elements are produced at depth in the star but during third dredge-up (TDU) episodes the convective envelope can penetrate inwards and carry to the surface the heavy elements synthesised in the He intershell. Consec-

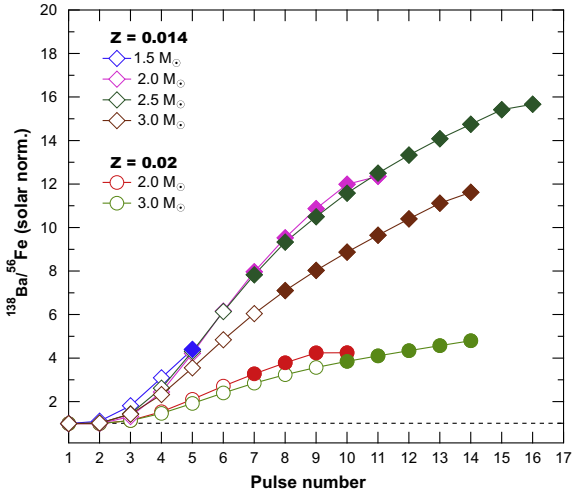

Fig. 9. Theoretical predictions of the evolution of ^{138}Ba relative to seed nuclei (e.g. ^{56}Fe) in the envelopes of AGB stars as a function of thermal pulse number. Each thermal pulse with third dredge-up provides more of the *s*-process nuclides into the stellar envelope. Stellar models of AGB stars of masses $M = 1.5$, 2.0, 2.5, and 3.0 $M_{\odot}$ for metallicity $Z = 0.014$ and stars of masses $M = 2.0$ and 3.0 $M_{\odot}$ for metallicity $Z = 0.02$ (Cristallo et al., 2009, 2011; FRUITY database). Filled symbols corresponds to C/O > 1 in the stellar envelope. Solar abundances from Lodders (2003).

utive TDU episodes lead to *s*-process enriched material being mixed into the convective envelope leading to a progressive enrichment of heavy elements in the stellar photosphere. The dredge-up also results in more carbon being brought to the surface of the star, which can create a C-rich environment as required for the condensation of SiC.

Stellar model predictions for the REE *s*-process enrichment in the envelope of low-mass AGB stars are shown in Figs. 9 and 10. These predictions represent the mixing between two components, one close to the solar composition, representing the initial composition of the stellar envelope, the other with isotopic characteristics close to those predicted for pure *s*-process. The magnitude of the departure from the initial composition depends on the efficiency and the number of mixing cycles (TDU).

Theoretical predictions were computed with the FUNS code (FUll Network Evolutionary Code; Straniero et al., 2006). Several updates have followed and are extensively discussed in Cristallo et al. (2009, 2011, 2015). Here, we present the model predictions for the envelope compositions of AGB stars of masses 1.5, 2.0, 2.5, and 3.0 $M_{\odot}$ for metallicity $Z = 0.014$ and masses 2.0 and 3.0 $M_{\odot}$ for metallicity $Z = 0.02$. The models presented have been selected for C/O > 1 in the envelope so that the condition for the formation of SiC is satisfied. The stellar envelope becomes able to condense SiC after 5, 7, 7, and 8 thermal pulses with TDU in the 1.5, 2.0, 2.5, and 3.0 $M_{\odot}$ for metallicity $Z = 0.014$, respectively, and after 7 and 10 thermal pulses with TDU in the 2.0 and 2.5 $M_{\odot}$ for metallicity $Z = 0.02$, respectively.

In Fig. 9, the normalised ^{138}Ba abundance ([Ba/Fe] = $(\text{Ba/Fe})_{s\text{-process}}/(\text{Ba/Fe})_{\odot}$) is plotted relative to the seed

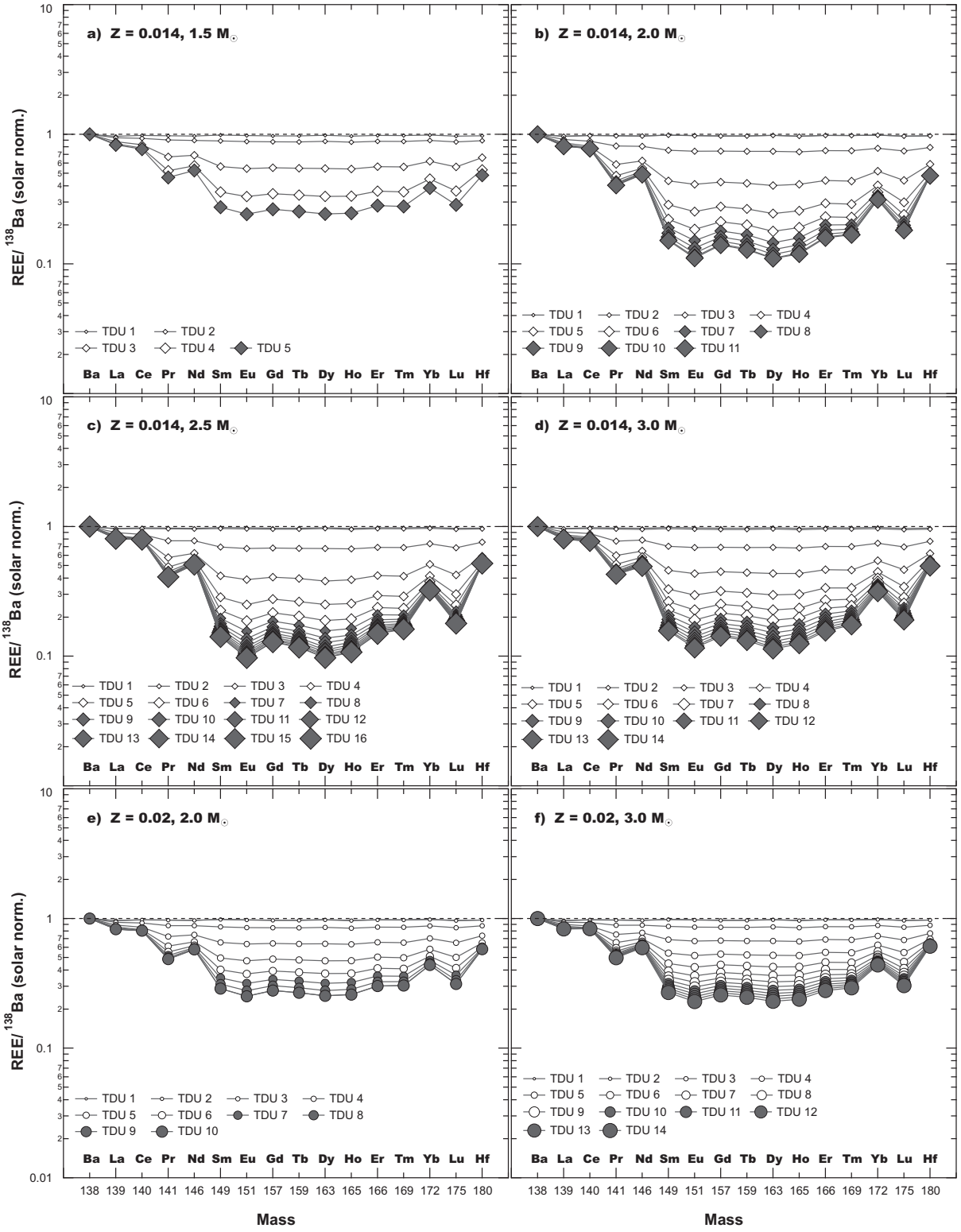

Fig. 10. Stellar abundances of the AGB envelope of the measured isotopes of REE and Hf doubly normalised to the abundance of ^{138}Ba and to solar abundances. All cases show the progressive enrichment of Ba relative to the neighbouring REE as thermal pulses with TDU proceed. Stellar models of AGB stars of masses $M = 1.5$, 2.0, 2.5, and 3.0 $M_{\odot}$ for metallicity $Z = 0.014$ and stars of masses $M = 2.0$ and 3.0 $M_{\odot}$ for metallicity $Z = 0.02$ (Cristallo et al., 2009, 2011; FRUITY database). Filled symbols corresponds to C/O > 1 in the stellar envelope. Solar abundances from Lodders (2003).

nuclei (e.g. ^{56}Fe) versus the number of TDU cycles. In all stellar models, the AGB envelope becomes progressively enriched in Ba with each TDU cycle. In Fig. 10, stellar model predictions for REEs relative to Ba are shown. Plotted are the stellar abundances of the AGB envelope of the measured isotopes of REE and Hf, doubly normalised to the abundance of ^{138}Ba and to solar abundances. All cases show the progressive enrichment of Ba relative to the neighbouring REE associated with the AGB TDU. This is due to the building of the Ba-La-Ce-Pr isotopes associated with the $n = 82$ magic neutron number peak, with ^{138}Ba having the greatest enrichment. The lowest REE abundances are in the Eu to Ho mass range. The patterns consistently show smooth variation in the REE abundances, except for the case of ^{146}Nd, and maybe also ^{172}Yb, which both appear anomalously higher than the trend established by the adjacent REEs. For comparison, both ^{146}Nd and ^{172}Yb show lower neutron capture cross sections than the surrounding REEs (Fig. 8).

4.2. Interpreting trace-element abundances in presolar SiC

4.2.1. Normalisation to solar composition

The solar-normalised trace-element abundance pattern of presolar SiC (Fig. 7) suggests depletions in the most volatile trace elements Eu and Yb, and possibly an elevated abundance of Tm which could be suggestive of the removal of an ultra refractory component prior to condensation. Eu and Yb anomalies represent the incomplete condensation of these elements following condensation of SiC in the AGB stellar envelope.

Condensation calculations for major, minor, and trace elements, including some REEs, in C-rich envelopes have been presented by Lodders and Fegley (1995) (referred to below as LF95). Any potential for fractional condensation of the REEs was not evident in LF95 because only La, Ce, and Nd were modelled. Lodders and Fegley (1993) modelled REE condensation as sulphides, and specifically as a sulphide solid solution in CaS. While this may not be an appropriate analog for carbide substitution, it does indicate that YbS and EuS are the lowest temperature condensates and therefore a correlated deficit is consistent with a fractional condensation effect. In addition to La, Ce, and Nd, LF95 also modelled Ba condensation. Modelling of Ba shows that it has a lower condensation temperature than La-Ce-Nd in silicon carbide and so for complete condensation, equilibration of gas-solid to temperatures down to 1200 K are required, some 340 K below the condensation temperature of SiC.

This behaviour is quite analogous to hibonite chemistry (Ireland and Fegley, 2000). The REEs behave as refractory trace elements with enrichments up to ca. 100 x chondritic in PLAC hibonites (Ireland, 1988; Ireland et al., 1988), but Eu and Yb are depleted. Refractory trace elements Hf, Zr, Sc, and Y are enriched to similar levels as the refractory REE, while Sr, Ba, Nb, and V show lower normalised abundances. This is consistent with a volatility fractionation with Ba, Eu, and Yb staying in the gas phase during condensation of the hibonite precursors.

La/Ba abundances appear relatively unfractionated in the "Average SiC" composition shown in Fig. 7. However, this may be in part be an artefact of DTM-SiC analyses. For the DTM SiC mount, we noted that the initial count rates of Ba could be high and then rapidly decayed. As such the La/Ba could be quite variable even after the initial burn-in phase. The KJB analyses may be a better representation of Ba and light REE abundances. In this case, Ba is slightly lower than La in normalised abundance, consistent with some degree of Ba depletion. However, the effect is relatively small given the overall range of the REE abundances, and could also be subject to issues associated with the normalisation to solar abundances as opposed to a composition enriched in *s*-process nuclides.

As noted above, the Tm abundance appears to be higher than the interpolation between Er and Lu. A high Tm abundance is a characteristic for Group II refractory inclusions (Mason and Taylor, 1982). However, we note that the Hf abundance is not depleted, as would be the case for a Group II pattern resulting from the prior removal of an ultra refractory (e.g., HfC) component from the condensation region.

The issue with some of this interpretation is that it is based on a normalisation to the chondritic abundances of the isotopes of these elements, which are a combination of both *s*- and *r*-process nuclides. In the following section we re-normalise the abundances to an *s*-process composition and discuss the consequences.

4.2.2. Normalisation to s-process composition

From the models presented in Fig. 10, it is apparent that the *s*-process abundance pattern is not particularly sensitive to the exact model used. In essence this is because the abundance of the nuclides in the mains *s*-process path are mostly defined by the neutron capture cross sections of the (n, γ) reactions and the competing β reactions. However, the absolute shift away from solar composition towards the pure *s*-process abundance pattern is model dependent, for example, in models experiencing less TDU the whole abundance pattern is closer to solar. For comparison, in the models presented by Karakas and Lugaro (2016) the Ba enhancement is typically 3 times higher than shown in Fig. 9 (see Fig. 18 of Karakas and Lugaro, 2016) and the shift away from the solar pattern in Fig. 10 is comparable to that shown by the solar metallicity ($Z = 0.014$) models, even at metallicities twice solar ($Z = 0.03$).

The presolar SiC abundances are shown normalised to model predictions for the envelope compositions of AGB stars with a range of stellar masses and metallicities in Fig. 11. For each mass-metallicity case, only the final envelope composition after the last thermal pulse with TDU is shown. There is little difference in the various normalisations and specifically for comparison of solar metallicity ($Z = 0.014$) to the super-solar metallicity ($Z = 0.02$). The solar metallicity provides a better overall fit to the predictions (^{i}REE/^{138}Ba ≈ 1) compared to the super-solar normalisation, which tends to show an underproduction of the middle REE (Gd-Er). However, as mentioned above, this result is model dependent.

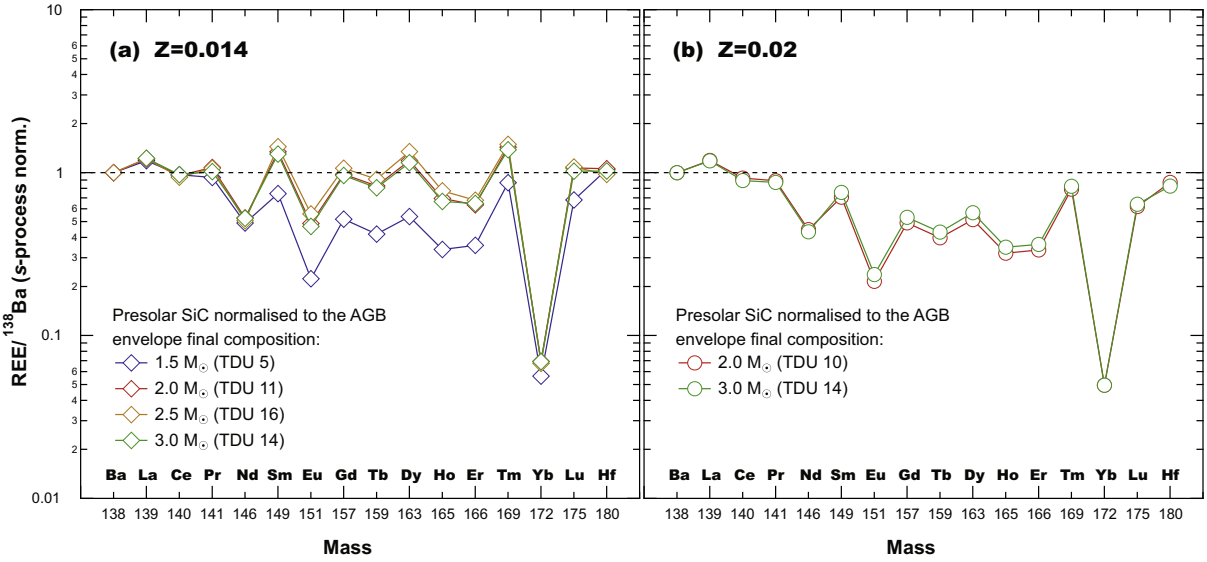

Fig. 11. Ba-REE-Hf abundances in presolar SiC normalised to *s*-process models covering a range of stellar masses for $Z = 0.014$ and 0.02. Only shown are normalisations to the AGB envelope compositions after the last TP with TDU. Measured SiC abundances show a good overall agreement with model predictions for the envelope compositions of AGB stars of 2–3 $M_{\odot}$ and solar metallicity. Exceptions are Eu and Yb, as seen in the solar normalised plot and likely due to incomplete condensation. The ^{146}Nd abundance derived here is in contrast to its location on the smooth curve relative to stellar abundances. See text for further discussion.

The overproduction of ^{146}Nd apparent in the AGB nucleosynthetic models (Fig. 10) also influences the abundances in the normalised data making ^{146}Nd appear anomalously low. Yin et al. (2006) also noted an anomalous abundance of ^{146}Nd but only of the order of ca. 15% relative to theoretical expectations of ^{146}Nd/^{144}Nd. Of note is that ^{144}Nd is used to normalise the data of Yin et al. (2006) and so there may be more than a simple issue with the nucleosynthetic predictions of ^{146}Nd, such as a systematic effect with Nd isotopes. The smooth pattern of La-Sm in the chondrite-normalised abundances in Fig. 7 (albeit fractionated), and a consistent trend in La-Sm (except Nd) in the *s*-process-normalised abundances, tend to support the implication that the ^{146}Nd (n, γ) capture cross section is not consistent with the observed presolar SiC abundances.

Any effect concerning the model predictions for ^{172}Yb are masked by the extremely large deficit in the Yb abundance evident in both the solar abundance normalisation and the *s*-process normalisation. This is similar to the abundance determined by Yin et al. (2006). Nevertheless, the nucleosynthetic model abundance of ^{172}Yb does appear to be anomalous relative to the trend of Er-Tm-Lu in Fig. 10. However, this is not a unique interpretation because it could be argued that ^{175}Lu is low relative to ^{172}Yb and ^{180}Hf.

Europium in the meteoritic SiC is low on the *s*-process normalised plots, but not as obviously low as on the chondrite-normalised plot. The ^{151}Eu abundance could be affected by the low apparent abundance of ^{146}Nd, however the distinct anomaly on the chondrite normalised plot suggests it is an issue of abundance brought about by volatility, rather than a distinct nucleosynthetic anomaly.

Normalisation to the *s*-process abundances allows us to evaluate the overall *s*-process path through the REE. As such we can evaluate models of *s*-process nucleosynthesis, including branching ratios, neutron densities, which are in turn affected by initial metallicity and stellar masses. However, it cannot be done in isolation. Deviations from theoretical abundances could be related to the nucleosynthesis of *s*-process nuclides or they could be due to thermal chemical fractionations (e.g. fractional condensation). Some systematic biases could even be induced by the use of a single nuclide in evaluating the overall abundance of the element in the SiC separate. For example, many of the isotopes examined are a mix of envelope, *s*-, and *r*-process nuclides and so the *s*-process signature cannot be examined in isolation without examining the overall isotopic composition of the element.

If we consider the *s*-process normalisation, there appear to be some issues with the abundances of Nd, Eu, Tm, and Yb. Of these, Eu and Yb are most likely related to fractional condensation, but we will consider each of these elements in turn in terms of potential *s*-process nucleosynthetic effects and implications for normalised abundances.

4.2.3. Neodymium

Neodymium has been evaluated previously for isotopic compositions both in "bulk" and as individual grains. Bulk analyses have been carried out by thermal ionisation mass spectrometry (TIMS), secondary ion mass spectrometry (SIMS), and inductively coupled plasma mass spectrometry (ICP-MS). The advantage of TIMS is that neodymium can be separated prior to analysis so that other REE isobars (i.e. ^{142}Ce, ^{148}Sm, ^{150}Sm) are not present. Hoppe and Ott (1997) have compiled the TIMS data for bulk separates. Zinner et al. (1991) were the first to provide SIMS data for Nd isotopes. Their data are obtained with energy filtering and so SiC clusters and molecules should not be an

issue. The Zinner et al. (1991) SIMS data are in good agreement with the TIMS data for Nd isotopes with $^{146}Nd/^{144}Nd$ agreeing within error.

Yin et al. (2006) used ICP-MS for analysis of a SiC-bearing slurry directly injected into the plasma source. Data for $^{146}Nd/^{144}Nd$ are consistent with the TIMS and SIMS data, but the $^{145}Nd/^{144}Nd$ appears to be elevated. Yin et al. (2006) noted that their terrestrial test samples were offset from "normal", and the meteoritic SiC analyses were likely offset in a similar fashion from the TIMS (terrestrial-*s*-process mixing line of Hoppe and Ott, 1997). Their interpretation was that there could be unidentified molecular interferences under ^{143}Nd and ^{145}Nd with overall contribution to isotope ratios of order 10%. Notwithstanding the possible issues with the ICP-MS ^{145}Nd data, the $^{146}Nd/^{144}Nd$ data is consistent between all methodologies. Therefore, the ^{146}Nd abundance determined during this work should be appropriate.

The Nd anomalies apparent in Fig. 10 (envelope compositions normalised to solar) and Fig. 11 (SiC compositions normalised to *s*-process predictions) are therefore related to the model predictions for the abundance of ^{146}Nd. We note that Yin et al. (2006) plotted Nd isotope compositions and showed that the Arlandini et al. (1999) $^{146}Nd/^{144}Nd$ ratio is elevated by ~15% compared to meteoritic SiC. Of relevance here, in the theoretical predictions from Arlandini et al. (1999) and those computed with the FUNS code (Cristallo et al., 2009, 2011, 2015) for which the neutron-capture cross section for ^{146}Nd is taken from Bao et al. (2000). A somewhat higher neutron-capture cross section would lead to a better agreement between the SiC data and the stellar predictions. We therefore conclude that the ^{146}Nd *s*-process deviation as presented may be an artefact caused by an overproduction of ^{146}Nd by stellar models and as such stellar theoretical predictions of this nuclide must be re-evaluated.

4.2.4. Europium

We have previously measured Eu isotopes in the KJB SiC bulk sample and single SiC grains (Ávila et al., 2013b). The $^{151}Eu/^{153}Eu$ SiC ratios are in good agreement with astronomical observations in carbon-enhanced metal poor (CEMP) stars enriched in *s*-process elements, despite the difference in metallicity between CEMP stars and those where the SiC condensed. The SiC $^{151}Eu/^{153}Eu$ ratio is, however, higher than model predictions. Ávila et al. (2013b) showed that the AGB model predictions can match the SiC data if an improved formalism to evaluate the contribution of excited nuclear states in the calculation of the $^{151}Sm(n, \gamma)$ stellar reaction rate is used. A higher production of ^{151}Eu can potentially reduce the deviation in the ^{151}Eu SiC composition from theoretical predictions. On the other hand, the observed ^{151}Eu depletions on SiC can be easily explained by volatility fractionation.

4.2.5. Thulium

The ^{169}Tm abundance we have determined, and shown relative to solar abundances in Fig. 7, appears to be potentially anomalously high. Evaluation of this is difficult because of the highly anomalous abundance of the adjacent element Yb. Thulium is mono isotopic (^{169}Tm) and so is not typically measured with TIMS because a suitable isotope spike for concentration determination is not available. Yin et al. (2006) provided estimates of an upper limit for its abundance with $^{169}Tm/^{144}Nd$ of 0.46.

There are potentially four issues with an accurate Tm abundance measurement. ***First*** is the augmentation of the signal by an isobaric interference. We feel this is unlikely given that the data have been acquired with a combination of high mass resolution and energy filtering so that molecules (notably oxides) and Si-C-O clusters are excluded. ***Second*** is the calibration to a relative sensitivity factor that could be in error. Again, we feel that this is unlikely. The RSF we have determined are similar to RSF values determined in previous work. While cosmochemical samples can show quite large Tm fractionations, terrestrial samples do not, and no significant Tm anomaly is expected nor observed for the precision available in our methodology. The ***third*** issue is related to the low number of counts accumulated and possible differences in signal resulting from data reduction. We have derived ratios in two discrete modes: evaluating isotope-ratio data as time dependent variables, and as a base reference, forming ratios from the total number of counts accumulated through the analysis. Both routines provide similar data so it does not appear likely to be a data reduction artefact. ***Fourth*** is that the excess Tm counts are real, such as from a Group II CAI contribution. However, this would have to be a very large CAI component and should be evident in depressed concentrations of Lu and Hf. A depletion in ultra-refractory Lu and Hf is not apparent and so we exclude this explanation. Still, a sort of nugget affect may be the most likely for providing the few extra counts that are apparent in the Tm signal.

4.2.6. Ytterbium

Only limited isotopic data is available for Yb. Yin et al. (2006) report $^{171}Yb/^{172}Yb$ and $^{173}Yb/^{172}Yb$ but the data are not consistent for the three measurements. The signals are low and isotopic interferences are also evident at adjacent mass positions. The main issue in carrying out Yb isotopic determinations is the low signal. We have not measured the isotopic composition of Yb. Nevertheless, we concur with Yin et al. (2006) that the extremely low abundance apparent for Yb is almost certainly related to its low elemental abundance in SiC rather than a nucleosynthetic effect.

4.3. Overall s-process pathway

Notwithstanding some of the apparently anomalous isotopic characteristics noted above, the REE abundances we have measured in meteoritic SiC are consistent with a closed nucleosynthetic pathway (Fig. 12). That is, the abundances through the pathway are consistent with progressive addition of neutrons and β decay to successive elements. Depletions in Eu and Yb appear to be a consequence of volatility and their apparent deficits are due to formation conditions, not nucleosynthetic production.

The initial stages of the *s*-process pathway through the REEs sticks to the magic neutron number ($n = 82$) isotones.

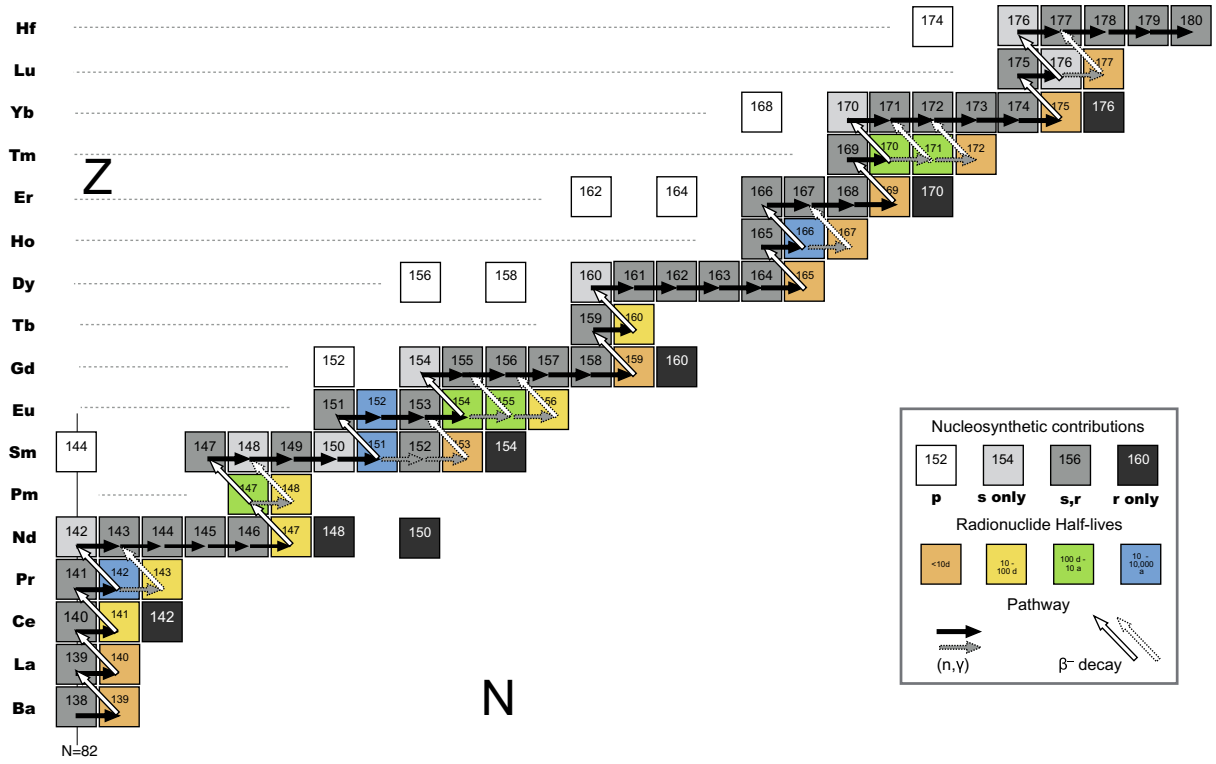

Fig. 12. *s*-Process nucleosynthetic pathway through the chart of the nuclides around the REE. Shown are the elements from $Z = 56$ (Ba) to $Z = 72$ (Hf). Also indicated is the neutron number (N) of $N = 82$ which is magic. The dominant pathway is shown with solid arrows for (n, γ) reactions and β decays. The arrows with broken borders indicate possible branches. Relevant radionuclides for the *s*-process pathway are shown in coloured boxes with colours according to half life. The *s*-process pathway reaches all possible *s*-process nuclides indicating that even long-lived radionuclide branches still provide populated β decay pathways to the lightest *s*-process isotope of an element. Format adopted from Walker et al. (1984).

From ^{138}Ba (n, γ) ^{139}Ba is a rapid decay to ^{139}La, followed by ^{140}La decay to ^{140}Ce. The abundance of ^{141}Pr indicates there can only be limited *s*-process production of ^{142}Ce (with the dominant path through decay of ^{141}Ce to ^{141}Pr; $t_{1/2}$ of 33 d). Neutron addition to build ^{142}Pr and its rapid decay takes the *s*-process path to ^{142}Nd.

Successive (n, γ) reactions then build the stable neodymium isotopes to ^{146}Nd. An active β decay branch at ^{147}Nd ($t_{1/2} = 11$ d) to ^{147}Pm and then ^{147}Sm is consistent with the low abundances of ^{148}Nd and ^{150}Nd in presolar SiC.

In turn, successive (n, γ) reactions build the stable samarium isotopes to ^{150}Sm. At ^{151}Sm ($t_{1/2} = 90$ a), there is a potential branching with β decay to ^{151}Eu, or neutron addition with ^{151}Sm(n, γ)^{152}Sm. As discussed in Ávila et al. (2013b), both ^{152}Sm and ^{151}Eu are present in presolar SiC indicating both neutron addition to ^{151}Sm leading to ^{152}Sm, and decay of ^{151}Sm to ^{151}Eu on the cessation of the neutron flux. Notwithstanding the specific activity of this branch, ^{153}Eu is either populated by ^{151}Eu(n, γ)^{152}Eu (n, γ)^{153}Eu or by β decay from ^{153}Sm (produced from ^{152}Sm(n, γ)^{153}Sm).

The radioactive Eu isotopes ^{154}Eu ($t_{1/2} = 8.5$ a), ^{155}Eu ($t_{1/2} = 4.7$ a), and ^{156}Eu ($t_{1/2} = 15$ d) could be populated by neutron addition providing various branches to the stable Gd isotopes. This branching will be addressed elsewhere. Gadolinium has stable isotopes on the *s*-process path from ^{154}Gd to ^{158}Gd, and so once the Eu branch decays to Gd, neutron reactions proceed to the heavier Gd isotopes. Neutron addition to produce ^{159}Gd ($t_{1/2} = 19$ h) leads to ^{159}Tb.

Neutron addition to ^{159}Tb leads to ^{160}Tb ($t_{1/2} = 72$ d) and decay to ^{160}Dy. Successive (n, γ) reactions lead to ^{164}Dy; ^{165}Dy ($t_{1/2} = 2.3$ h) decay leads to ^{165}Ho. Another neutron addition leads to ^{166}Ho, which has a relatively long half life of 1200 a and could be considered stable under conditions for neutron addition. However, the abundance of ^{166}Er indicates that the ^{166}Ho branch is active. Neutron addition to ^{167}Ho ($t_{1/2} = 3$ h) would lead to a branch to ^{167}Er bypassing ^{166}Er. As yet, little is known regarding Er isotope abundances in presolar SiC.

Erbium builds through successive (n, γ) reactions to the stable isotopes from ^{166}Er to ^{168}Er. The abundance of ^{169}Tm indicates that ^{169}Er ($t_{1/2} = 9.4$ d) decays rather than proceeding to ^{170}Er.

Successive neutron addition(s) to ^{169}Tm leads to possible competing branches to Yb from three Tm radioisotopes, viz. ^{170}Tm ($t_{1/2} = 129$ d) ^{170}Yb, ^{171}Tm ($t_{1/2} = 1.9$ a) ^{171}Yb, and ^{172}Tm ($t_{1/2} = 64$ h) ^{172}Yb. An accurate and precise measurement of the abundances of Yb isotopes in meteoritic SiC is required to assess these pathways.

Ytterbium builds through successive (n, γ) reactions from ^{170}Yb to ^{174}Yb, and then to ^{175}Yb ($t_{1/2} = 4.2$ d), which decays to ^{175}Lu. The ^{175}Lu(n, γ) reaction results in ^{176}Lu.

This is a stable isotope under terrestrial conditions but undergoes accelerated β decay under stellar conditions (Beer et al., 1981). The rapid decay is consistent with both the solar abundance of ^{176}Hf, and the modelled *s*-process abundances. Hf builds by successive (n, γ) build up from ^{176}Hf to ^{180}Hf. Finally the agreement in the presolar SiC abundance of ^{180}Hf with the modelled *s*-process composition, closes the *s*-process path for this mass region.

Overall, there is a remarkable consistency between the abundances of the measured *s*-process nuclides in the SiC with model predictions.

4.4. Formation of SiC in AGB winds

Eu and Yb abundance anomalies suggest that condensation of SiC has occurred prior to the temperatures of condensation of Eu and Yb being achieved. This then has consequences for the preservation of other elements in meteoritic SiC, or for the mechanism by which the elements were entrained in SiC.

The deficit in the abundances of Eu and Yb indicates that elements with similar condensation temperatures should be depleted. In hibonite inclusions, Ba, Sr, Nb, and V are depleted relative to the levels of the highly refractory REE. A depletion in Ba is not so noticeable in the presolar SiC patterns with Ba/La appearing similar for both solar-normalised and *s*-process normalised plots (Figs. 7 and 11). Amari et al. (1995) noted deficits in the abundance of Sr, but V, although having a much lower condensation temperature, was always of a similar abundance to refractory Ti.

As has been noted previously, the abundances of many elements must have been brought about through a mechanism other than incorporation during condensation. For example, the abundance of Xe, a noble gas with no propensity for bonding, and a very low condensation temperature, is remarkably high (Lewis et al., 1994). The most likely mechanism is implantation in the wind phase, and most likely ion implantation where ions are accelerated in stellar magnetic fields. For retention of Xe, this must have occurred after the grains were sufficiently cold, where cold can be defined by the closure temperature of rare gases in minerals. Pignatari et al. (2004) considered that the *s*-process Xe in SiC was most likely due to implantation related to cool and partly ionised winds during the AGB phase, as opposed to hot and strongly ionised winds in the Planetary Nebula phase.

5. SUMMARY AND CONCLUSIONS

The *s*-process pathway through the REEs has been determined by analysing trace element abundances in bulk samples of presolar SiC. Abundances were measured by secondary ion mass spectrometry (SHRIMP RG) using a combination of high mass resolution ($M/\Delta M_{10\%} = 12{,}000$) coupled with energy filtering to exclude higher order polyatomic Si-C-O clusters that are evident in the mass region of the REEs. REE and Hf abundances were normalised relative to $^{138}Ba^{+}$ in NIST SRM 610. Relative sensitivity factors for REE/Ba and Hf/Ba appear to be appropriate for SiC as demonstrated by analysis of REE in a synthetic trace element bearing SiC ceramic.

The measured abundances of Ba, Hf, and the refractory REE (La-Sm, Gd-Er, and Lu) are in excellent agreement with model predictions for the envelope compositions of AGB stars of 2–3 $M_{\odot}$ and metallicity close to solar. However, the model predictions for ^{146}Nd appear to be high suggesting that one or more cross sections for nuclides involved in its production may need re-examination. Tm appears marginally high in normalised abundance, but this does not appear to be related to the Group II REE (ultra-refractory depleted) pattern because Lu and Hf are not depleted. The Tm abundance is prone to nugget effects because of the very low number of counts detected.

Eu and Yb are depleted relative to other REE. This is similar to the Group III pattern found in refractory inclusions and suggests that the silicon carbide grains condensed while Eu and Yb remained in the gas phase. This is consistent with depletions in Sr noted by Amari et al. (1995), however, other less-refractory trace elements (e.g. Ba, V) do not show this depletion. The depletion of Eu and Yb, and the presence of volatile elements (e.g. Xe) in meteoritic SiC indicates that these elements must be incorporated when the SiC grains have cooled and most likely by ion implantation.

ACKNOWLEDGEMENTS

This work is dedicated to our friend and colleague Ernst Zinner. Ernst provided guidance, friendship, mentoring, constructive criticism, grounding, acumen. He was an instrumentalist, an analyst, a modeller and a theoretician. The Milky Way will not be the same without him. TRI acknowledges support from the Australian Research Council– Australia grants DP0342772 and DP0666751. LN and CA acknowledge support from NASA grant NNX10AI63G.

APPENDIX A. SUPPLEMENTARY DATA

Supplementary data associated with this article can be found, in the online version, at http://dx.doi.org/10.1016/j.gca.2017.05.027.

REFERENCES

Alexander C. M. O'D. and Nittler L. R. (1999) The galactic evolution of Si, Ti, and O isotopic ratios. *Astrophys. J.* **519**, 222–235.

Amari S., Lewis R. S. and Anders E. (1994) Interstellar grains in meteorites: I. Isolation of SiC, graphite, and diamond; size distributions of SiC and graphite. *Geochim. Cosmochim. Acta* **58**, 459–470.

Amari S., Hoppe P., Zinner E. and Lewis R. S. (1995) Trace element concentrations in single interstellar SiC grains from the Murchison meteorite. *Meteoritics* **30**, 679–693.

Amelin Y., Kaltenbach A., Iizuka T., Stirling C. H., Ireland T. R., Petaev M. I. and Jacobsen S. B. (2010) U-Pb chronology of the solar system's oldest solids with variable $^{238}U/^{235}U$. *Earth Planet. Sci. Lett.* **300**, 343–350.

Anders E. and Zinner E. (1993) Interstellar grains in primitive meteorites: diamond, silicon carbide, and graphite. *Meteorit. Planet. Sci.* **28**, 490–514.

Arlandini C., Käppeler F., Wisshak K., Gallino R., Lugaro M., Busso M. and Straniero O. (1999) Neutron capture in low-mass asymptotic giant branch stars: cross sections and abundance signatures. *Astrophys. J.* **525**, 886–900.

Ávila J. N., Lugaro M., Ireland T. R., Gyngard F., Zinner E., Cristallo S., Holden P., Buntain J., Amari S. and Karakas A. (2012) Tungsten isotopic compositions in stardust SiC grains from the Murchison meteorite: constraints on the s-process in the Hf-Ta-W-Re-Os region. *Astrophys. J.* **744**, 49–62.

Ávila J. N., Ireland T. R., Gyngard F., Zinner E., Malmann G., Holden P. and Amari S. (2013a) Barium isotopic compositions in large stardust SiC grains from the Murchison meteorite: a cautionary tale of unresolved mass interferences. *Geochim. Cosmochim. Acta* **120**, 628–647.

Ávila J. N., Ireland T. R., Lugaro M., Gyngard F., Zinner E., Cristallo S., Holden P. and Rauscher T. (2013b) Europium s-process signature at close-to-solar metallicity in stardust SiC grains from asymptotic giant branch stars. *Astrophys. J. Lett.* **768**, L18.

Ávila J. N., Ireland T. R., Lugaro M., Gyngard F. and Karakas A. (2016) Gadolinium and dysprosium isotopic compositions in presolar SiC grains from the Murchison meteorite. In Abstract, 79th Annual Meeting of the Meteoritical Society, #6318.

Bao Z. Y., Beer H., Käppeler F., Voss F., Wisshak K. and Rauscher T. (2000) Neutron cross sections for nucleosynthesis studies. Atom. Data Nucl. Data Tables **76**, 70–154.

Beer H., Käppeler F., Wisshak K. and Ward R. A. (1981) ^{176}Lu: cosmic clock or stellar thermometer?. *Astrophys. J. Supp.* **46** 295–317.

Bernatowicz T., Fraundorf G., Tang M., Anders E., Wopenka B., Zinner E. and Fraundorf P. (1987) Evidence for interstellar SiC in the Murray carbonaceous meteorite. *Nature* **330**, 728–730.

Boynton W. V. (1975) Fractionation in the solar nebula: condensation of yttrium and the rare earth elements. *Geochim. Cosmochim. Acta* **39**, 569–584.

Cristallo S., Straniero O., Gallino R., Piersanti L., Domínguez I. and Lederer M. T. (2009) Evolution, nucleosynthesis, and yields of low-mass asymptotic giant branch stars at different metallicities. *Astrophys. J.* **696**, 797–820.

Cristallo S., Piersanti L., Straniero O., Gallino R., Domínguez I., Abia C., Di Rico G., Quintini M. and Bisterzo S. (2011) Evolution, nucleosynthesis, and yields of low-mass asymptotic giant branch stars at different metallicities. II. The FRUITY database. *Astrophys. J. Suppl. Ser.* **197**, 17.

Cristallo S., Straniero O., Piersanti L. and Gobrecht D. (2015) Evolution, nucleosynthesis, and yields of AGB stars at different metallicities. III. Intermediate-mass models, revised low-mass models, and the pH-FRUITY interface. *Astrophys. J. Suppl. Ser.* **219**, 40.

Hoppe P. and Ott U. (1997) Mainstream silicon carbide grains from meteorites. In Astrophysical Implications of the Laboratory Study of Presolar Materials AIP Conf. Proc. (ed. T. J. Bernatowicz and E. Zinner). vol. 402, pp. 27–58.

Hoppe P., Amari S., Zinner E., Ireland T. R. and Lewis R. S. (1994) Carbon, nitrogen, magnesium, silicon, and titanium isotopic compositions of single interstellar silicon carbide grains from the Murchison carbonaceous chondrite. *Astrophys. J.* **430**, 870–890.

Ireland T. R. (1988) Correlated morphological, chemical, and isotopic characteristics of hibonites from the Murchison carbonaceous chondrite. *Geochim. Cosmochim. Acta* **52**, 2827–2839.

Ireland T. R. (1990) Presolar isotopic and chemical signatures in hibonite-bearing refractory inclusions from the Murchison carbonaceous chondrite. *Geochim. Cosmochim. Acta* **54**, 3219–3237.

Ireland T. R. (1995) Ion microprobe mass spectrometry: techniques and applications in cosmochemistry, geochemistry, and geochronology. In *Advances in Analytical Geochemistry*, vol. 2 (eds. M. Hyman and M. Rowe). JAI Press, pp. 1–118.

Ireland T. R. and Fegley, Jr., B. (2000) The solar system's earliest chemistry: systematics of refractory inclusions. *Int. Geol. Rev.* **42**(10), 865–894.

Ireland T. R. and Bukovanska M. (2003) The initial ^{182}Hf/^{180}Hf of the solar system determined from meteoritic zircons. *Geochim. Cosmochim. Acta* **67**, 4849–4856.

Ireland T. R., Fahey A. J. and Zinner E. K. (1988) Trace-element abundances in hibonites from the Murchison carbonaceous chondrite: constraints on high-temperature processes in the solar nebula. *Geochim. Cosmochim. Acta* **52**, 2841–2854.

Ireland T. R., Zinner E. K. and Amari S. (1991) Isotopically anomalous Ti in presolar SiC from the Murchison meteorite. *Astrophys. J. Lett.* **376**, L53–L56.

Ireland T. R., Clement S., Compston W., Foster J. J., Holden P., Jenkins B., Lanc P., Schram N. and Williams I. S. (2008) The development of SHRIMP. *Aust. J. Earth Sci.* **55**, 937–954.

Karakas A. I. and Lugaro M. (2016) Stellar yields from metal-rich asymptotic giant branch models. *Astrophys. J.* **825**, 26.

Lewis R. S., Amari S. and Anders E. (1994) Interstellar grains in meteorites: II. SiC and its noble gases. *Geochim. Cosmochim. Acta* **58**, 471–494.

Liu M.-C., McKeegan K. D., Goswami J. N., Marhas K. K., Sahijpal S., Ireland T. R. and Davis A. M. (2009) Isotopic records in CM hibonites: implications for timescales of mixing of isotope reservoirs in the solar nebula. *Geochim. Cosmochim. Acta* **73**, 5051–5079.

Liu N., Savina M. R., Davis A. M., Gallino R., Straniero O., Gyngard F., Pellin M. J., Willingham D. G., Dauphas N., Pignatari M., Bisterzo S. and Herwig F. (2014) Barium isotopic compositions of mainstream silicon carbide grains from Murchison: constraints for s-process nucleosynthesis in asymptotic giant branch stars. *Astrophys. J.* **786**, 66.

Liu N., Savina M. R., Gallino R., Davis A. M., Bisterzo S., Gyngard D., Käppeler F., Cristallo S., Dauphas N., Pellin M. J. and Dillmann I. (2015) Correlated strontium and barium isotopic compositions of acid-cleaned single mainstream silicon carbides from Murchison. *Astrophys. J.* **803**, 12.

Lodders K. (2003) Solar system abundances and condensation temperatures of the elements. *Astrophys. J.* **591**, 1220–1247.

Lodders K. and Fegley B. (1993) Lanthanide and actinide chemistry at high C/O ratios in the solar nebula. *Earth Planet. Sci. Lett.* **117**, 125–145.

Lodders K. and Fegley B. (1995) The origin of circumstellar silicon carbide grains found in meteorites. *Meteoritics* **30**, 661–678.

Lugaro M., Davis A. M., Gallino R., Pellin M. J., Strainer O. and Käppeler F. (2003) Isotopic compositions of strontium, zirconium, molybdenum, and barium in single presolar SiC grains and Asymptotic Giant Branch stars. *Astrophys. J.* **593**, 486–508.

Mason B. and Taylor S. R. (1982) Inclusions in the Allende meteorite: Smithson. *Contrib. Earth Sci.* **25**, 1–39.

Nguyen A. N., Nittler L. R., Alexander C. M. O'D. and Hoppe P. (2018) Titanium isotopic compositions of rare presolar SiC grain types from the Murchison meteorite. *Geochim. Cosmochim. Acta* **221**, 162–181.

Nicolussi G. K., Pellin M. J., Lewis R. S., Davis A. M., Amari S. and Clayton R. N. (1998) Molybdenum isotopic composition of individual presolar silicon carbide grains from the Murchison meteorite. *Geochim. Cosmochim. Acta* **62**, 1093–1104.

Nittler L. R. and Alexander C. M. O'D. (2003) Automated isotopic measurements of micron-sized dust: application to meteoritic presolar silicon carbide. *Geochim. Cosmochim. Acta* **67**, 4961–4980.

Pignatari M., Gallino R., Straniero O. and Davis A. (2004) The origin of xenon trapped in presolar mainstream SiC grains. *Men. S. A. It.* **75**, 729–734.

Podosek F. A., Prombo C. A., Amari A. and Lewis R. S. (2004) *s*-Process Sr isotopic compositions in presolar SiC from the Murchison Meteorite. *Astrophy. J.* **605**, 960–965.

Savina M. R., Davis A. M., Tripa C. E., Pellin M. J., Clayton R. N., Lewis R. S., Amari S., Gallino R. and Lugaro M. (2003) Barium isotopes in individual presolar silicon carbide grains from the Murchison meteorite. *Geochim. Cosmochim. Acta* **67**, 3201–3214.

Straniero O., Gallino R. and Cristallo S. (2006) S-Process in low-mass asymptotic giant branch stars. *Nucl. Phys. A* **777**, 311–339.

Tian W., Chen B., Ireland T. R., Green D. H., Suzuki K. and Chu Z. (2011) Petrology and geochemistry of dunites, chromitites and mineral inclusions from the Gaositai Alaskan-type complex, North China Craton: implications for mantle source characteristics. *Lithos* **127**, 165–175.

Walker F. W., Miller D. G. and Feiner F. (1984) *Chart of the Nuclides*, 13th ed. General Electric Company, p. 59.

Yin Q.-Z., Lee C.-T. A. and Ott U. (2006) Signatures of the s-process in presolar silicon carbide grains: Barium through Hafnium. *Astrophys. J.* **647**, 676–684.

Zinner E. (1998) Stellar nucleosynthesis and the isotopic composition of presolar grains from primitive meteorites. *Ann. Rev. Earth Planet. Sci.* **26**, 147–188.

Zinner E. (2004) Presolar grains. In *Treatise on Geochemistry*, vol. 1 (eds. K. K. Turekian, H. D. Holland and A. M. Davis). Elsevier, Oxford and San Diego, pp. 17–39.

Zinner E., Amari S. and Lewis R. S. (1991) *S*-process Ba, Nd, and Sm in presolar SiC from the Murchison meteorite. *Astrophys. J. Lett.* **382**, L47–L50.

Zinner E. and Crozaz G. (1986) A method for the quantitative measurement of rare earth elements in the ion microprobe. *Int. J. Mass Spectrom. Ion Proc.* **69**, 17–38.

Associate editor: Anders Meibom